JGR Atmospheres

RESEARCH ARTICLE
10.1029/2024JD042206

The Turbulent Pressure Spectrum Within the Roughness Sublayer of a Subarctic Forest Canopy

Toprak Aslan[1], Gabriel G. Katul[2], and Mika Aurela[1]

[1]Finnish Meteorological Institute, Helsinki, Finland, [2]Department of Civil and Environmental Engineering, Duke University, Durham, NC, USA

Key Points:

- Low-cost commercial sensors were used to measure turbulent static pressure variations above a subarctic forest
- A new logarithmic scaling with height was derived for the turbulent static pressure variance
- Turbulent pressure spectra predictions for small and large eddy sizes agree with the measurements in their resolved range

Correspondence to:

T. Aslan,
toprak.aslan@fmi.fi

Citation:

Aslan, T., Katul, G. G., & Aurela, M. (2025). The turbulent pressure spectrum within the roughness sublayer of a subarctic forest canopy. *Journal of Geophysical Research: Atmospheres*, *130*, e2024JD042206. https://doi.org/10.1029/2024JD042206

Received 20 AUG 2024
Accepted 27 DEC 2024
Corrected 20 JUN 2025

This article was corrected on 20 JUN 2025. See the end of the full text for details.

Abstract The turbulent static pressure spectrum $E_{pp}(k_x)$ as a function of longitudinal wavenumber k_x in the roughness sublayer of forested canopies is of interest to a plethora of problems such as pressure transport in the turbulent kinetic energy budget, pressure pumping from snow or forest floor, and coupling between flow within and above canopies. Long term static pressure measurements above a sub-arctic forested canopy for near-neutral conditions during the winter and spring were collected and analyzed for three snow cover conditions: trees and ground covered with snow, trees are snow free but the ground is covered with snow, and snow free cover. In all three cases, it is shown that $E_{pp}(k_x)$ obeys the attached eddy hypothesis at low wavenumbers $(1/\delta < k_x < 1/z)$—with $E_{pp}(k_x) \propto u_*^4 k_x^{-1}$ and Kolmogorov scaling in the inertial subrange at higher wavenumbers—with $E_{pp}(k_x) \propto \epsilon^{4/3} k_x^{-7/3}$, where u_* is the friction velocity at the canopy top, ϵ is the mean turbulent kinetic energy dissipation rate, z is the distance from the snow top, and δ is the boundary layer depth. The implications of these two scaling laws to the normalized root-mean squared pressure $C_p = \sigma_p/u_*^2$ and its newly proposed logarithmic scaling with normalized wall-normal distance z/δ are discussed for snow covered and snow free vegetation conditions. The work here also shows that the k_x^{-1} in the $E_{pp}(k_x)$ appears more extensive and robust than its longitudinal velocity counterpart.

Plain Language Summary Textbook definitions of pressure at a point microscopically relate it to the collision frequency of molecules around a hypothetically small volume. Macroscopically, however, pressure couples distant regions of a fluid as may be demonstrated when opening a door rapidly in a closed room and noting movement of a curtain or water level variations in a water closet. For these macroscopic reasons, time variations in static pressure near the top of a forested canopy are of interest to a variety of atmospheric problems because they can move air volumes rapidly in and out of the canopy volume, soil, or snow cover. Yet, there is no accepted theory to describe these variations, which are necessary for mathematically representing their effects on biosphere-atmosphere exchanges in climate models. The work here offers a phenomenological model that predicts the static pressure variability as well as the contributions of different swirling motion or eddies to this variability. The model is tested using low-cost commercial static pressure sensors across a wide range of snow cover conditions with agreement between model predictions and measurements.

1. Introduction

Static pressure fluctuations are at the core of the equations of fluid motion; yet, their spectral scaling properties are less understood compared with their velocity counterparts in turbulent flows. This difficulty is partly attributed to measurement challenges that continue to plague studies of static pressure fluctuations at high Reynolds numbers (Elliott, 1972; Sigmon et al., 1983; Tsuji et al., 2007) and partly due to theoretical challenges. In atmospheric research, studies on turbulent static pressure fluctuations are commonly motivated by their role in (a) the transport terms within the turbulent kinetic energy budget (Kaimal & Finnigan, 1994; Maitani & Seo, 1985; McBean & Elliott, 1975; Wyngaard & Coté, 1971), (b) the pressure strain correlation terms that redistribute turbulent energy among the three fluctuating velocity components - sometimes labeled as the "Robin Hood" effect (George et al., 1984) because those terms take energy from the energy-rich component and pass it to the energy-poor components, and (c) pressure gradients that spectrally link small scale to organized motion (Albertson et al., 1998; A. Thomas & Bull, 1983) as well as physically coupling distant regions of the flow (Tsuji et al., 2007) as may occur between the canopy air volume and the overlying atmosphere (Raspet & Webster, 2015; Shaw & Zhang, 1992; Sigmon et al., 1983; Zhuang & Amiro, 1994). The spectral properties of turbulent static pressure are also receiving attention in many other geophysical research applications. In climate research, pressure pumping from soils, forest floor, and snow surfaces are receiving renewed interest (Burns et al., 2021; Colbeck, 1989;

Kimball & Lemon, 1970; W. Massman et al., 1995, 1997; Takle et al., 2004). Pressure pumping within snow or soil occurs at multiple time scales—ranging from fractions of seconds (i.e., turbulent) to several days (W. Massman et al., 1997; W. J. Massman & Frank, 2022; Takle et al., 2004). Some studies report minor impact on mass exchange between snow or soil and the atmosphere by turbulent pressure pumping (Hubbard et al., 2005; W. Massman et al., 1997; W. J. Massman & Frank, 2022; Suzuki et al., 2006), whereas others report significant effects (> 40% of mass transport) (Bowling & Massman, 2011; Laemmel et al., 2019; Seok et al., 2009; Swanson et al., 2005; Takagi et al., 2005). Similar enhancements due to the so-called non-diffusive transport (mainly vertical advection due to pressure pumping) have been reported for forest floor carbon dioxide fluxes (Maier et al., 2010; Roland et al., 2015). Likewise, vapor transport from soils has been shown to be enhanced by turbulent pressure (Farrell et al., 1966) but other studies do not support significant enhancement (W. J. Massman & Frank, 2022).

In hydraulics and aquatic ecology, mass, momentum, and heat exchanges within the so-called hyporheic zone are facilitated by turbulent pressure fluctuations that lead to transmission rates orders of magnitude larger than their Darcian matrix counterpart (Boano et al., 2014; Boulton et al., 1998). Above porous beds (e.g., gravel beds in streams), pressure fluctuations near the permeable interface not only impact the flow within the bed but also lead to adjustments in the relation between the so-called Darcy-Weisbach friction factor and the bulk Reynolds number above the bed (Manes et al., 2012). Another general application of static pressure fluctuations is in air-water mass and momentum exchanges across such an interface. When airflow occurs over a water surface, fluctuations in air static pressure can contribute to the generation of water waves (Phillips, 1957). This generation occurs by means of a resonance mechanism in which a component of the "energetic" mode of the surface pressure spectrum moves at the same speed as the free surface wave with the same wave number. In numerous engineering applications such as structural vibrations and acoustic propagation, static pressure statistics are also necessary and those have been reviewed in a number of studies (Fritsch et al., 2023; Goody, 2004). The role of pressure fluctuations within urban roughness elements as well as within wind farms is receiving renewed attention given the role of pressure in building ventilation and efficiency of wind turbines (Cortina et al., 2016; Hirose et al., 2020).

Among the earliest theories for the turbulent static pressure spectrum and its root-mean squared value (σ_p) were developed for homogeneous and isotropic turbulence in the late 1940s (Batchelor, 1951; Heisenberg, 1948). In those theories, the pressure correlation function was linked to a quantity closely related to the fourth order velocity increment moments (Gotoh & Nakano, 2003; Hill & Wilczak, 1995; Monin & Yaglom, 1975). When employing Kolmogorov scaling (Kolmogorov, 1991) to those fourth-order velocity increments, it was possible to arrive at an explicit spectral shape for the pressure spectrum (or its Fourier pair, the pressure auto-covariance function), which when integrated across scales, yields a relation between pressure- and velocity-variances (Batchelor, 1951; Heisenberg, 1948; Hill & Wilczak, 1995; Kraichnan, 1956; Obukhov & Yaglom, 1959; Pearson & Antonia, 2001; Uberoi, 1953). However, those approaches have not considered the shape of the static pressure spectrum at low wavenumbers in the presence of a rough canopy, which is the main focus here.

The primary goal of the work here is to arrive at a spectral shape for the turbulent pressure fluctuations that can be readily employed in future analysis or models where high-frequency pressure fluctuations need to be represented. The sought mathematical complexity for the pressure spectra ought to resemble those derived for the Kansas experiments (Kaimal & Finnigan, 1994) for velocity in terms of simplicity, making synthetic generation of turbulent pressure fluctuations convenient for integration into large-scale models. The proposed form will be tested against newly acquired pressure measurements from low-cost commercial sensors in the roughness sub-layer above a tall subarctic canopy for snow covered and snow-free conditions. During snow-covered periods, tree crowns appear more slender and smoother compared with their snow free counterparts. Hence, the presence and absence of snow offers a natural manipulation of roughness cover without altering tree spacing and mean tree height—only crown size and its local roughness. As a logical starting point for this inquiry, near-neutral atmospheric conditions will be the main focus here to permit comparisons with published laboratory studies and direct numerical simulations. Those conditions are also prevalent above rough forested canopies for a wide range of snow cover conditions.

The manuscript is organized as follows: The theory section begins with the governing equations and reviews what is known about the scaling laws of the pressure spectrum across various eddy sizes spanning the very large scales, production scales, inertial scales, and very fine scales. Findings from laboratory experiments with limited

Reynolds numbers, along with scaling analysis and basic theories are also covered. Following this review, a simplified model for the turbulent pressure variance is derived showing its similarity to the so-called attached eddy model for adiabatic conditions. The experimental details about the site conditions used to explore the pressure spectra and variances, the pressure measurements, and run selection are presented. The results and discussion comparing model calculations (spectral and variances) with measurements are then featured. The role of the canopy in damping the spectral shapes of the pressure is elaborated upon. Conclusions and future work plans are then provided. Comparisons between the low-cost high-frequency pressure measurements here and standard pressure measurements as well as an exploration of possible temperature contamination effects are presented in the appendix.

2. Theory

2.1. Definitions

The Cartesian coordinate system used defines x_i with $x_1 = x, x_2 = y$, and $x_3 = z$ as the longitudinal, lateral, and vertical directions, respectively, with $z = 0$ being the ground surface. The longitudinal ($i = 1$) direction is aligned along the mean wind direction defined locally at z. The instantaneous velocity components along x, y, and z directions are labeled as u_i with $u_1 = u, u_2 = v$, and $u_3 = w$, respectively, and overline defines time averaging over some period T_p selected here to be 1,800 s. The $\overline{U}$ represents the mean velocity over T_p at z. Turbulent fluctuations from their time-averaged values are indicated by primed quantities. The potential temperature θ is also needed in the quantification of thermal stratification and can be decomposed into a mean $\overline{\theta}$ and a fluctuating or θ' term. The buoyancy parameter linking density to temperature fluctuations is defined as $\beta = g/\overline{\theta}$, where g is the gravitational acceleration and $1/\overline{\theta}$ is the coefficient of thermal expansion of an ideal gas. The turbulent stress τ_t above the canopy is related to the friction velocity $u_* = \sqrt{\tau_t/\rho_o}$, where ρ_o is the mean air density. The local u_* above the canopy is determined from the overall turbulent stresses

$$u_* = \left(\overline{u'w'}^2 + \overline{v'w'}^2\right)^{1/4}. \tag{1}$$

The spectrum of an arbitrary fluctuating flow variable s' satisfies the normalizing property

$$\sigma_s^2 = \int_0^\infty F_{ss}(k_x)\, dk_x; \tag{2}$$

where k_x is the one-dimensional (longitudinal) wavenumber in space derived from Taylor's frozen turbulence hypothesis (Hsieh & Katul, 1997; Taylor, 1938; Wyngaard & Clifford, 1977) and given as $k_x = 2\pi n/\overline{U}$, n is the natural frequency (cycles per period), and $F_{ss}(k_x)$ is the spectral density function. Thus, k_x may be viewed as a characteristic eddy size and $F_{ss}(k_x)$ measures the strength of variability in s' associated with k_x.

Turbulent flows in the near-neutral atmospheric surface layer (ASL) are dominated by eddies with wide-ranging sizes. The largest eddies tend to scale with the boundary layer height (an outer-layer scale) that may be approximated by Arya (1981), Clarke (1970), and McBean (1976)

$$\delta = A_\delta \frac{u_*}{f}, \tag{3}$$

where $f = 1.4 \times 10^{-4}$ rad s^{-1} is the Coriolis parameter for the site here and $A_\delta = 0.2$ is a constant though its value can range from 0.1 to 0.3. The finest scales of turbulence are in the regime where the action of kinematic viscosity ν becomes significant and those fine scales are represented by the Kolmogorov micro-scale given by

$$\eta = \left(\frac{\nu^3}{\epsilon}\right)^{1/4}, \tag{4}$$

where ϵ is the mean turbulent kinetic energy dissipation rate (overline is dropped for notational simplicity). In classical boundary layer theories, eddies attached to the ground are presumed to be responsible for diffusive

exchanges and they scale as $l_m = \kappa(z - d)$ (i.e., inner-layer scale), where $\kappa = 0.4$ is the von Kármán constant and d is the zero-plane displacement (Kaimal & Finnigan, 1994; Tennekes & Lumley, 1972). There are other length scales that dominate momentum exchange just above the canopy top—such as mixing layer eddies (Raupach et al., 1996) and combinations of attached eddies and mixing layer eddies (Poggi et al., 2004) whose relative contribution to an effective l_m depends on the leaf area density. These canonical length scales (micro-, inner-, and outer- scales) have been used to delineate key "break-points" in the pressure spectra, where scaling laws shift their exponents.

For pragmatic purposes, a balance between mechanical production and viscous dissipation of turbulent kinetic energy is assumed here, which is reasonable for near neutral conditions in stationary and planar homogeneous flow in the absence of subsidence and transport terms (Charuchittipan & Wilson, 2009; Katul et al., 2011; Saddoughi & Veeravalli, 1994; Salesky et al., 2013). From this turbulent kinetic energy balance, ϵ is given by

$$\epsilon = u_*^2 \frac{d\overline{U}}{dz} = \frac{u_*^3}{l_m}. \tag{5}$$

Replacing this estimate in Equation 4 and re-arranging enables the definition of a Reynolds number Re_+ given by

$$\frac{l_m}{\eta} = \left(\frac{u_* l_m}{\nu}\right)^{3/4} = Re_+^{3/4}. \tag{6}$$

Likewise, an estimate of the largest (i.e., δ) to the finest (i.e., η) scale, a measure of the widest scale separation, is given by

$$\frac{\delta}{\eta} = \frac{\delta}{l_m}\frac{l_m}{\eta} = A_\delta \frac{u_*}{f l_m} Re_+^{3/4} = \frac{A_\delta}{f}\frac{d\overline{U}}{dz} Re_+^{3/4}. \tag{7}$$

This estimate underscores that δ/l_m is dictated by the ratio of the mean flow vorticity $\left(d\overline{U}/dz\right)$ and the Coriolis time scale (f). Last, the finest scales of turbulence defined by the Kolmogorov velocity $v_K = (\epsilon\nu)^{1/4}$ and η result in a micro-scale Reynolds number

$$Re_\eta = \frac{v_K \eta}{\nu} = 1, \tag{8}$$

Meaning that molecular viscosity ν and the turbulent viscosity $v_K\eta$ are equally important to the energetics of the flow at such fine scales (Tennekes & Lumley, 1972).

Another common Reynolds number used in wind tunnel experiments is the bulk friction-based Reynolds number given by $Re_\tau = u_*\delta/\nu$. This Reynolds number can be evaluated as

$$Re_\tau = \frac{A_\delta}{f}\frac{u_*^2}{\nu} = \frac{\delta}{\eta} Re_+^{1/4}. \tag{9}$$

Thus, Re_τ does sense the largest to the finest eddy sizes in the boundary layer but with a sub-unity scaling enhancement arising from $Re_+^{1/4}$. In atmospheric boundary layer turbulence, $Re_\tau \sim 10^7$, 3–4 orders of magnitude larger than wind tunnel experiments or Direct Numerical Simulations.

2.2. Governing Equation

The turbulent pressure $p'(t, x_i)$ satisfies the Poisson equation given by Hanjalić and Launder (1972), Launder et al. (1975)

$$\frac{1}{\rho_o}\nabla^2 p' = \overbrace{-2\frac{\partial \overline{U_i}}{\partial x_j}\frac{\partial u_j'}{\partial x_i}}^{\text{Rapid Term}} \overbrace{-\frac{\partial^2}{\partial x_i \partial x_j}\left(u_i' u_j' - \overline{u_i' u_j'}\right)}^{\text{Slow Term}} + \overbrace{\frac{g}{\overline{\theta}}\frac{\partial \theta'}{\partial z}}^{\text{Buoyancy Term}}. \tag{10}$$

This equation is elliptic—meaning that p' at position x_i and time t requires knowledge of the flow field and temperature across the entire flow domain. Despite this complexity, Equation 10 underscores two mechanisms that historically formed the basis for much of the models for p'. The first is known as the "rapid term" because it involves direct interaction between the mean strain rate $\left(\partial \overline{U_i}/\partial x_j\right)$ and turbulence. The second is known as the "slow term" because it involves turbulent stresses that require some time to adjust after the mean strain rate reacts to changes in boundary conditions. The third term is the buoyancy pressure and does not respond instantly to changes in the mean shear or the mean temperature gradient. However, it does respond instantly to changes in temperature gradients caused by density fluctuations, and thus shares some similarities with the rapid term. Because the focus is on near-neutral conditions, the buoyancy term is hereafter ignored.

Some of the early experiments and model calculations suggest that the rapid term is dominant (Corcos, 1964; Panton & Linebarger, 1974) for the determination of $\sigma_p^2 = \overline{p'^2}$. In the case where surface layer scaling applies, meaning that z and u_* are the only characteristic length and velocity scale, and upon ignoring thermal stratification and the "slow" term, dimensional considerations applied to Equation 10 suggest that the non-zero mean velocity gradient (the only non-zero source term in the Laplace equation) is for $i = 1$ and $j = 3$. Thus, the contribution of the rapid term to the pressure variance may be of the order of Katul et al. (1996).

$$\frac{1}{\rho_o}\frac{\sigma_p}{z}\frac{}{z} \sim \frac{u_*}{z}\frac{u_*}{z}. \tag{11}$$

A $\sigma_p = \rho_o C_p u_*^2$ (Batchelor, 1951) is recovered where C_p is the pressure coefficient and is of order unity (Katul et al., 1996). For wall-bounded flow, C_p values are in the range of 2.1–6.0 as discussed elsewhere (Blake, 1970; Elliott, 1972; Farabee & Casarella, 1991; Willmarth, 1975). Another possibility is to assume the finest scales of turbulence dominate the effects of the instantaneous gradient on σ_p^2. That is, the overall characteristic velocity and length scales of turbulent velocity gradients are comparable to σ_w and η. This assumption suggests that the rapid term involving $\partial w'/\partial x$ contributes to the pressure variance as $\sigma_w/\eta \sim (u_*/z)\, Re_+^{3/4}$, which leads to

$$\frac{1}{\rho_o}\frac{\sigma_p}{z}\frac{}{z} \sim \frac{u_*}{z}\frac{u_*}{z} Re_+^{3/4}. \tag{12}$$

With such analysis, $\sigma_p = \rho_o C_p u_*^2$ but with C_p increasing with increasing $Re_+^{3/4}$. These two choices (i.e., z and η) for the appropriate length scale determining the effects of $\partial w'/\partial x$ on σ_p^2 bound all other possibilities when the rapid term dominate. It will be shown later that models based on the spectral shape for $E_{pp}(k_x)$ result in a non-constant C_p that vary with $\log(z/\delta)$. Henceforth, the pressure is normalized by ρ_o and only kinematic variables are employed in the spectral analysis next.

2.3. The Static Pressure Spectrum

The scaling laws of $E_{pp}(k_x)$ across various eddy sizes, flow conditions, and generation-dissipation mechanisms are now considered.

2.3.1. The Inertial Sub-Range

As a starting point, homogeneous isotropic turbulence is considered. For such a case, the micro-scales v_k and η are used as normalizing variables (Tennekes & Lumley, 1972). This scaling leads to a non-dimensional form of $E_{pp}(k_x)$ given by Tsuji et al. (2007)

$$\frac{E_{pp}(k_x)}{v_K^4 \eta} = \frac{E_{pp}(k_x)}{\epsilon^{3/4}\nu^{7/4}} = \phi_p(k_x\eta), \tag{13}$$

where $\phi_p(k_x\eta)$ is a dimensionless similarity function to be determined. In the inertial subrange where $k_x z \gg 1$ but $k_x\eta \ll 1$, the effects of viscosity are no longer relevant to the dynamics of $E_{pp}(k_x)$ and must be canceled out from Equation 13. The elimination of ν from Equation 13 requires a unique $\phi_p = C_{p1}(k_x\eta)^{-7/3}$ thereby resulting in

$$E_{pp}(k_x) = C_{p1}\epsilon^{4/3}k_x^{-7/3}, \tag{14}$$

where C_{p1} is a similarity coefficient presumed to be constant and universal. There is experimental support for a $k_x^{-7/3}$ scaling in the inertial subrange of atmospheric flows (Elliott, 1972; W. Massman et al., 1997; Ould-Rouis et al., 1996; Zhao et al., 2016). Moreover, Equation 14 has been tested for turbulent wakes and jets at inertial subrange scales (deemed locally isotropic) and was also shown to be valid (Ould-Rouis et al., 1996). Equation 14 has also been evaluated using direct numerical simulations for isotropic turbulence (Gotoh & Fukayama, 2001; Gotoh & Rogallo, 1999; Tsuji & Ishihara, 2003; Xu et al., 2007), large eddy simulations (Alvelius & Johansson, 2000; Miles et al., 2004) and other theories based on locally homogeneous turbulent flows (Hill & Wilczak, 1995). It is no coincidence that the $E_{pp}(k_x) \sim k_x^{-7/3}$ emerges for the inertial subrange as the turbulence-turbulence interaction term (or slow term) may be significant to the pressure spectrum thereby making $E_{pp}(k_x)$ exhibit scaling laws similar to $E_{uw}(k_x)$ (George et al., 1984; Katul et al., 2013; Kim, 1989; Miles et al., 2004; Raspet & Webster, 2015).

2.3.2. The Dissipation Range

The transition from the inertial to the viscous dissipation range occurs at around $k\eta = 10$ for the turbulent kinetic energy and pressure spectra (Ould-Rouis et al., 1996; Zhao et al., 2016), though this limit is rarely resolved in field experiments reporting $E_{pp}(k_x)$. Some theories suggest a sharp exponential cut-off in the viscous range (Hill & Wilczak, 1995; Zhao et al., 2016). Empirical models also suggest $E_{pp}(k_x) \sim k_x^{-5}$ (Goody, 2004) but reviewing those models are outside the scope here. Given the rapid decay of the spectrum with increasing k_x (i.e., much faster than $k_x^{-7/3}$), the viscous sub-range is no longer considered here as its contribution to pressure variances is deemed negligible compared with the inertial scales or large scales.

2.3.3. Large Scales

Unlike the inertial and dissipation regimes, there is no accepted universal spectral theory describing the pressure in wall-bounded flows or canopy flows at large scales. For homogeneous turbulence, numerical simulations suggest that at low k_x (Gotoh & Fukayama, 2001)

$$\frac{E_{pp}(k_x)}{\epsilon^{4/3}L_p^{7/3}} = \phi_L(k_x L_p), \tag{15}$$

where L_p is an integral scale for the pressure fluctuations and $\phi_L(.)$ is another similarity function to be determined. There are two possible choices for L_p: an inner layer scaling where $L_p = z$ and an outer layer scaling where $L_p = \delta$, the boundary layer depth. When $k_x L_p \gg 1$ and $k_x z \ll 1$, then an overlap region must exist where $E_{pp}(k_x)$ is independent of L_p. This condition in the overlap region is used to determine $\phi_L(.)$ by eliminating L_p resulting in

$$\phi_L(k_x L_p) = \frac{E_{pp}(k_x)}{\epsilon^{4/3}L_p^{7/3}} = \frac{A_o}{k_x L_p}, \tag{16}$$

where A_o is a similarity coefficient and ϵ scales as $u_*^2(u_*/L_p)$. This choice of ϕ_L leads to a model for the pressure spectrum at large scales given by

$$E_{pp}(k_x) = A_o\epsilon^{4/3}L_p^{7/3}(k_x L_p)^{-1} = C_{p2}\left(\frac{u_*^3}{L_p}\right)^{4/3}L_p^{7/3}\left(\frac{1}{k_x L_p}\right), \tag{17}$$

where C_{p2} is another similarity coefficient. With this choice for $\phi_p(k_x L_p)$, Equation 15 reduces to

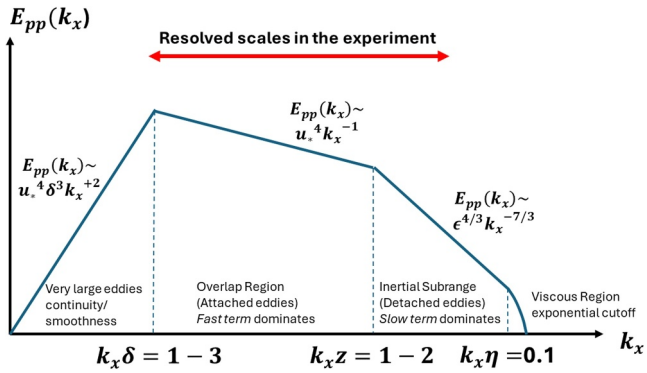

Figure 1. Summary of the scaling laws in the turbulent pressure spectrum $E_{pp}(k_x)$ as a function of the longitudinal wavenumber k_x within the inertial (or log) region of a turbulent boundary layer. The transition wavenumbers between differing scaling regimes are based on laboratory experiments or direct numerical simulations. A possible transition region from k_x^{-1} to the $k_x^{-7/3}$ identified in some studies (Albertson et al., 1998; Tsuji et al., 2007) is not shown for clarity.

$$E_{pp}(k_x) = C_{p2} u_*^4 k_x^{-1}. \tag{18}$$

The $E_{pp}(k_x) \propto k_x^{-1}$ was already speculated using the inactive eddy motion hypothesis (Bradshaw, 1967; Panton & Linebarger, 1974; Tsuji et al., 2007). Direct numerical simulations in channel flows also demonstrate the existence of a k_x^{-1} scaling for $k_x\delta > 1$ (Kim, 1989) when the static pressure is analyzed in the log-layer. Large eddy simulations of the atmospheric boundary layer also revealed an extensive k_x^{-1} scaling at scales larger than z for the overlap region in near-neutral conditions (Ding et al., 2018). Low-frequency pressure spectra reported in smooth and rough-wall boundary layers exhibited a k_x^{-1} region for $k_x\delta > 2$ (Blake, 1970). Wind tunnel data generally suggest a slower roll-off of the surface pressure with a scaling regime that is commensurate with a $k_x^{-0.7}$ (Goody, 2004; Tsuji et al., 2007). However, for the same data sets, the pressure fluctuations measured in the overlap region exhibited an extensive k_x^{-1} scaling (Fritsch et al., 2023; Tsuji et al., 2007). A number of field experiments also report a k_x^{-1} scaling in the near-neutral ASL (Katul et al., 1996; Wei et al., 2021).

2.3.4. Very Large Scales

There are empirical models summarizing the shape of the turbulent pressure spectrum in the limit of $k_x\delta \to 0$. One common form is given by Goody (2004)

$$E_{pp}(k_x) = C_{p2} u_*^4 \delta (k_x\delta)^{+2}, \tag{19}$$

which is expressed by us as such to match the spectrum in the overlap region spectrum at $k_x\delta = 1$ (i.e., continuity constraint). There are a number of derivations leading to a k_x^2 scaling in this limit, perhaps the earliest proposed in 1954 (Ogura & Miyakoda, 1954). The one selected here is based on a statistical constraint: spatial spectra must vanish (i.e., $E_{pp}(k_x) \to 0$ at $k_x \to 0$ and at $k_x \to \infty$). The viscous cut-off ensures the latter is satisfied given the rapid spectral decay is much faster than $k_x^{-7/3}$ (usually on the order of k_x^{-5} (Goody, 2004; Joseph et al., 2020) to k_x^{-7} (Kim, 1989)). For the former, a constraint on the spectrum must be formulated to ensure that, at minimum, a continuity and smoothness condition is satisfied so that both $E_{pp}(k_x) \to 0$ and $dE_{pp}(k_x)/dk_x \to 0$ as $k_x \to 0$. These two conditions generally require $E_{pp}(k_x) \sim k_x^2$. The $E_{pp}(k_x) \sim k_x^2$ shape may also not be realized in the "real" atmosphere as large-scale meteorological processes, gravity waves, turbulence, and acoustic waves all contribute to alterations of the pressure spectrum at those scales (Marty et al., 2021). However, in zero-pressure gradient turbulent boundary layer experiments, there is experimental evidence that $E_{pp}(k_x) \sim k_x^2$ (Fritsch et al., 2023; Goody, 2004). In the absence of any alternative model, this scaling will be assumed to represent turbulent pressure fluctuations only for the very large scales.

Figure 1 summarizes all the predicted exponents and their associated mechanisms for the different range of scales for $E_{pp}(k_x)$. The work here will be focused on the overlap region and part of the inertial subrange that can be interrogated by the pressure sensors to be later described. Transients and other large scale (i.e., non-turbulent) meteorological drivers impacting the turbulent pressure spectrum will be "filtered" out prior to comparisons between model predictions and measurements.

2.3.5. Deviations From Inertial Subrange Scaling

At the transition from production to the inertial subrange, the effects of the integral scale may still have some impact on the scaling laws. Thus, one possible approach to accommodate them is to revise the inertial subrange pressure spectrum to be expressed as

$$E_{pp}(k_x) = C_{p1} \epsilon^{4/3} k_x^{-7/3} (k_x L_p)^{\mu_p}, \tag{20}$$

where μ_p remains to be determined. Some studies already reported $\mu_p = 2/3$ (Albertson et al., 1998; Mayor et al., 2023)). Others proposed that $\phi_p(k_x\eta)$ is not a constant due to finite Reynolds number effects, which may even lead to bottle-necks or a bump in the compensated spectrum (Tsuji et al., 2007). The $\phi_p(k_x\eta)$ argument is suggestive that viscous effects can persist up to scales commensurate with the inertial subrange for low Reynolds numbers encountered in some laboratory experiments and simulations.

An entirely different line of inquiry for the deviations from $k_x^{-7/3}$ and k_x^{-1} is through a refinement put forth by Kolmogorov, labeled as K62 (Kolmogorov, 1962). For the log-normal model of turbulent kinetic energy dissipation, the pth moment of the dissipation rate is related to the mean dissipation rate (i.e., ϵ) using (Boffetta et al., 2009)

$$\overline{\epsilon^p} = Q_o(\epsilon)^p Re_\lambda^{\beta_p}; \beta_p = \frac{3}{4}\mu_o(p^2 - p), \tag{21}$$

for any statistical moment $p > 0$, where Q_o depends on external conditions generating the turbulence, β_p is derived from the log-normal model of K62 with μ_o being the intermittency parameter of the dissipation rate. This parameter, in principle, is related to the power-law exponent of the spatial auto-correlation function of the turbulent kinetic energy dissipation rate (about 0.25–0.30 for internal intermittency only), $Re_\lambda = \sigma_u\lambda/\nu$ is the Taylor micro-scale Reynolds number formed from a macro-velocity $\sigma_u = \left(\overline{u'^2}\right)^{1/2}$, and $\lambda = \sigma_u\sqrt{15\nu/\overline{\epsilon}}$ is the Taylor micro-scale (Tennekes & Lumley, 1972). For $p = 4/3$, $\beta_p = \mu_o/3$, and C_{p1} and A_o vary with $Re_\lambda^{\mu_o/3}$, a non-constant. Recalling that $\lambda \sim \left(\eta^2 L_p\right)^{1/3}$, both large and micro-scale effects can impact A_o or C_{p1} as already speculated elsewhere (Albertson et al., 1998; Tsuji et al., 2007). Thus, the analysis here is suggestive that the compensated spectrum, expressed as

$$k_x^{7/3}\frac{E_{pp}(k_x)}{\epsilon^{4/3}} \propto (k_x L_p)^{\mu_o/9}(k_x\eta)^{2\mu_o/9}, \tag{22}$$

might be able to foreshadow how intermittency impacts the scaling laws in the overlap region and in the inertial subrange region. The point to be made here is that intermittency effects arising from averaging $\epsilon^{4/3}$ lead to spectral decay rates that are "flatter" (i.e., less steep in absolute value) than $-7/3$ in the inertial subrange and flatter than -1 in the overlap region. A flatter than k_x^{-1} scaling was noted as early as 1970 from an overlooked field experiment above a corn canopy at different stages of crop height (Kimball & Lemon, 1970). In those field studies, the reported shapes for the high frequency component were $E_{pp}(k_x) \sim k_x^{-6/3}$, which is also flatter than $-7/3$. Interestingly, field experiments over shrubs do report a near k_x^{-1} scaling at low wavenumbers but a k_x^{-2} scaling in the inertial subrange (Wei et al., 2021). Another experiment measuring near surface atmospheric pressure report a $k_x^{-5/3}$ scaling in the inertial subrange (Mayor et al., 2023) instead of $k_x^{-7/3}$ though no explanation was offered. Last, the data sets reported for wakes, jets, and the atmospheric boundary layer also show small deviations from $k_x^{-7/3}$ (less steep), which were speculated to be due to intermittency effects (Ould-Rouis et al., 1996).

2.4. A Logarithmic Scaling for Pressure Variances

Neglecting momentarily the effects of intermittency (i.e., setting $\mu_o = 0$) and accepting a k_x^{-1} scaling at low wavenumbers, continuity of the spectrum at $k_x = \beta/z$ results in $C_{p2} = C_{p1}(\beta\kappa_v)^{-4/3}$, where β is a constant delineating the transition from inactive eddies to inertial subrange (Huang & Katul, 2022). To link the spectral model to C_p, the normalizing property

$$\sigma_p^2 = \int_0^\infty E_{pp}(k_x)\,dk_x = \int_0^{1/\delta} C_{p2}u_*^4\delta^3 k_x^2 dk_x + \int_{1/\delta}^{\beta/z} C_{p2}u_*^4 k_x^{-1} dk_x + \int_{\beta/z}^\infty C_{p1}\epsilon^{4/3}k_x^{-7/3}dk_x \tag{23}$$

to yield

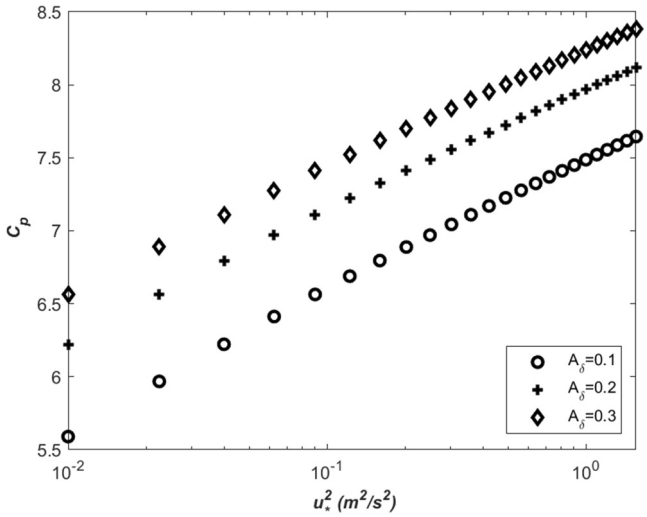

Figure 2. Modeled C_p with u_*^2 using Equation 26 for $\beta = 2$, $C_{p1} = 8$, $\kappa_v = 0.4$, $f = 1.4\times10^{-4}\text{s}^{-1}$, and $A_\delta = 0.1$, 0.2, and 0.3.

$$\sigma_p^2 = \frac{C_{p2}}{3}u_*^4 + C_{p2}u_*^4\log\left(\frac{\beta\delta}{z}\right) + \frac{3}{4}\frac{C_{p1}}{(\kappa_v\beta)^{4/3}}u_*^4, \tag{24}$$

which simplifies to

$$\frac{\sigma_p^2}{u_*^4} = C_{p2}\left[\frac{1}{3} + \frac{3}{4} - \log\left(\frac{z}{\beta\delta}\right)\right], \tag{25}$$

and is a form of a log-linear scaling similar to Townsend's attached eddy hypothesis for σ_u^2/u_*^2 (Banerjee & Katul, 2013; Huang & Katul, 2022; Marusic et al., 2013; Townsend, 1976). There are a number of laboratory studies that report profiles of σ_p supporting log-linear variations with z (Tsuji et al., 2007). Here, the contribution from the $(k_x\delta)^2$ regime are small compared with their inertial subrange counterpart (at least by a factor of 2) and perhaps the precise shape of the spectrum in this regime may not be as relevant for variance models. Hence, the final expression for the sought C_p is now given by

$$C_p^2 = \frac{\sigma_p^2}{u_*^4} = \frac{C_{p1}}{(\beta\kappa_v)^{4/3}}\left[\frac{13}{12} - \log\left(\frac{fz}{\beta A_\delta u_*}\right)\right]. \tag{26}$$

For locally isotropic turbulence, $C_{p1} = 8$ (Gotoh & Fukayama, 2001) and this value will be used throughout here. In several laboratory boundary layer flows, a $C_p = 3.4$ was reported (Blake, 1970). Thus, values exceeding $C_p = 3.4$ may be attributed to some large-scale modulations of $E_{pp}(k_x)$ or large deviations from local isotropy. As discussed elsewhere (Panton & Linebarger, 1974), scaling laws in pressure appear robust to the isotropy assumption (Panton & Linebarger, 1974). Predictions from Equation 26 are used to demonstrate the range of expected values for the canonical spectral shape already discussed. In these calculations, $C_{p1} = 8$ as derived from direct numerical simulation (DNS) for isotropic turbulence, and $\beta = 2$ as later shown from the spectral analysis. The calculations from Equation 26 are shown in Figure 2. The model calculations suggest that C_p can vary from 5.5 (at low u_* and $A_\delta = 0.1$) to 8.5 (at high u_* and $A_\delta = 0.3$). Interestingly, a C_p as large as 6.75 was put forth using the inactive eddy motion argument (Bradshaw, 1967). Likewise, wind-tunnel experiments did report a $C_p = 6.5$ for high Reynolds number boundary layers (Farabee & Casarella, 1991). Early theories using the rapid term only also estimate $C_p = 6$ (Kraichnan, 1956; Willmarth, 1975), close to the values predicted here when $A_\delta = 0.1$ and moderate u_*. Moreover, a C_p dependency on z/δ, or alternatively, a Reynolds number dependence was noted in early modeling studies (Panton & Linebarger, 1974) and few turbulent boundary layer experiments (Farabee & Casarella, 1991). These experiments suggest an increasing C_p with increasing Reynolds number consistent with the arguments here and the outcome of Equation 26. Atmospheric surface layer experiments for near-convective conditions indicate that $C_p^2 = 18(-z/L)^{2/3}$ (Wilczak & Businger, 1984). When extrapolating the same data set to near-neutral conditions, a $C_p^2 = 15$ was determined (Wilczak & Businger, 1984), which is some 4 times larger than the value reported in early wind tunnel experiments. The authors attributed this large C_p to thermal fluctuations persisting even for near-neutral conditions. Another possible explanation is the role of the logarithmic correction arising from z/δ given the large δ expected in such experiments. Large values of C_p (=13) were also reported from Large Eddy Simulation studies in the bottom 20% of the lower-atmosphere (Ding et al., 2018).

There are instances where low-frequency pressure modulations occur due to meso-scale or other non-turbulent motion that disrupt expected scaling relations. These disruptions have been reported in earlier studies of ground pressure situated at a forest floor (Sigmon et al., 1983). More recently, near ground measurements of turbulent pressure fluctuations in a grass field report a $k_x^{-5/3}$ in $E_{pp}(k_x)$ with deviations from this scaling associated with time scales longer than 2 min (Mayor et al., 2023). Local topographic variations can also generate large-scale static pressure fluctuations under certain wind conditions that are more energetic than their turbulent-only counterpart. Those instances must be filtered out when considering turbulent static pressure only. For this

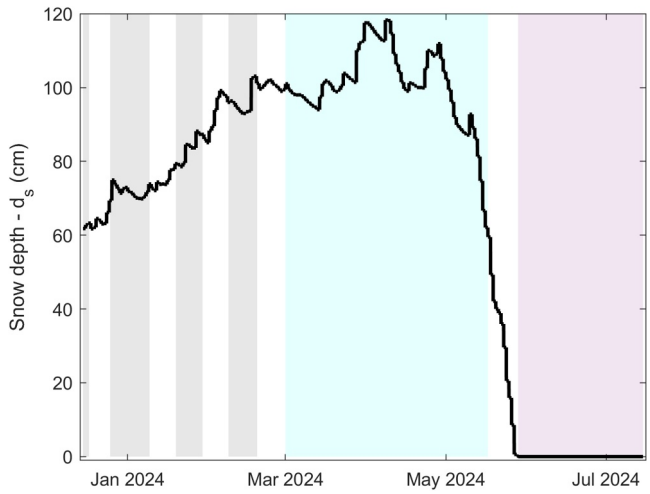

Figure 3. Snow depth (d_s) during the measurement period (15 December 2023–14 July 2024). The snow conditions are marked as shaded areas in the background as *all snow* in gray, *ground snow* in cyan, and *snow-free* in purple.

reason, the measured pressure fluctuations time series to be analyzed were decomposed into turbulent and non-turbulent components. A spectral cut-off filter set to 5 min was used to separate the largest turbulent scale from non-turbulent low-frequency motion. The precise numerical value of this filter cut-off was found not to be essential for near-neutral conditions provided it varies between 5 and 10 min. Plausibility arguments regarding a 5 min cut-off are now provided. In a flux-variance analysis reported by Waterman et al. (2022), how to separate turbulent from non-turbulent motion was explored using high-frequency data from the National Ecological Observatory Network (NEON) database. It was shown that for 39 sites (spanning short crops to forests) and multiple years per site, a 5 min cut-off recovered flux-variance relations and similarity constants well when compared to standard values (Waterman et al., 2022). This finding implies that a weak non-stationarity associated with non-turbulent motion was contributing to enhanced variances. Micro-meteorological studies that partition evapotranspiration into evaporation and transpiration, a low-frequency cut-off that varied from 5 to 10 min was also shown to be necessary so as to achieve acceptable convergence given the use of flux-variance similarity in these schemes (Zahn et al., 2022). In studies of mass, energy, and momentum transporting eddies over heterogeneous forested sites, it was reported that the time scale associated with the largest flux-bearing eddy was few minutes (C. Thomas et al., 2006) suggestive that eddies much longer than this time scale were surrogates to non-stationarity (i.e., non-turbulent). In ogive analysis for momentum and scalar fluxes at several sites, more than 90% of total fluxes were shown to be carried by time scales smaller than 5 min in the near-neutral limit (Sakai et al., 2001). All these studies hint that time scales much longer than 5 min are non-turbulent and likely contribute to non-stationarity in the time series and this non-stationarity has disproportionate impact on variances instead of turbulent fluxes.

3. Experiment

The study site (Kenttärova forest) is located within a subarctic region in northern Finland (67°59.237'N, 24°14.579'E) at an elevation of 347 m a.s.l (Aurela et al., 2015). The forest mainly consists of Norway spruce (Hylocomium-Myrtillus type, HMT) with a mean stand density of 643 stems per hectare, dominant tree height (h) of 14 m, and leaf area index (LAI) of 2.1 (no significant seasonal change). The site is under snow-cover for most of the year, starting in mid-October, reaching a peak in late-March and melting occurs in late-May (Meriö et al., 2023). During the study period (15 December 2023–14 July 2024), snow depth (d_s) gradually increased from ca. 60 to ca. 120 cm at its peak by the beginning of April, and snow cover fully melted away by late May, as shown in Figure 3. Considering its effect on roughness characteristics, the data are separated into three categories, that is, *all snow*, *ground snow,* and *snow-free*. *All snow* represents the snow cover on both trees and ground, which typically occurs following a heavy snow fall with persistently below freezing temperature conditions (Figure 4e). Succeeding *all snow*, alternating air temperature above freezing conditions cause the melting of snow on trees first, resulting in *ground snow* condition (Figure 4f), where cases with d_s>60 cm are considered for uniformity.

The micro-meteorological setup consists of (a) a conventional eddy covariance system located above the canopy at 23 m ($\doteq z$) above the soil surface, employing an ultrasonic three-dimensional anemometer (model USA-1; METEK GmbH, Elmshorn, Germany) and an enclosed-path nondispersive infrared gas analyzer (LI-7000, LI-COR Biosciences, USA), (b) a sonic anemometer (model USA-1; METEK GmbH, Elmshorn, Germany) located in the trunk space at 2.4 m height from the soil surface, (c) absolute barometric pressure sensors (BMP581, BOSCH, Germany) at 2.4 and 23 m above the soil surface (Figures 4b–4d). The pressure sensors were placed in a polycarbonate mounting enclosure (165 × 115 × 40 mm), where a polyurethane sampling tube with 20 cm length and 6 mm diameter linked the sensor and free atmosphere at the bottom of the enclosure as shown in Figure 4h. The BMP581 is a precision pressure sensor with dimensions 2 × 2 × 0.75 mm and with a relative accuracy of 6 Pa and a noise level of 0.08 Pa at the highest sampling rate (∼ 480 Hz). Since the interest here is pressure fluctuations and spectra not pressure gradients, the noise level is the pertinent criterion. The manufacturer also reports a temperature coefficient offset of ±0.5 Pa/K. Thus, comparisons between the BMP581 and a conventional slow-response pressure sensor used in standard weather stations (PTB220, Vaisala, Finland) as well as an assessment

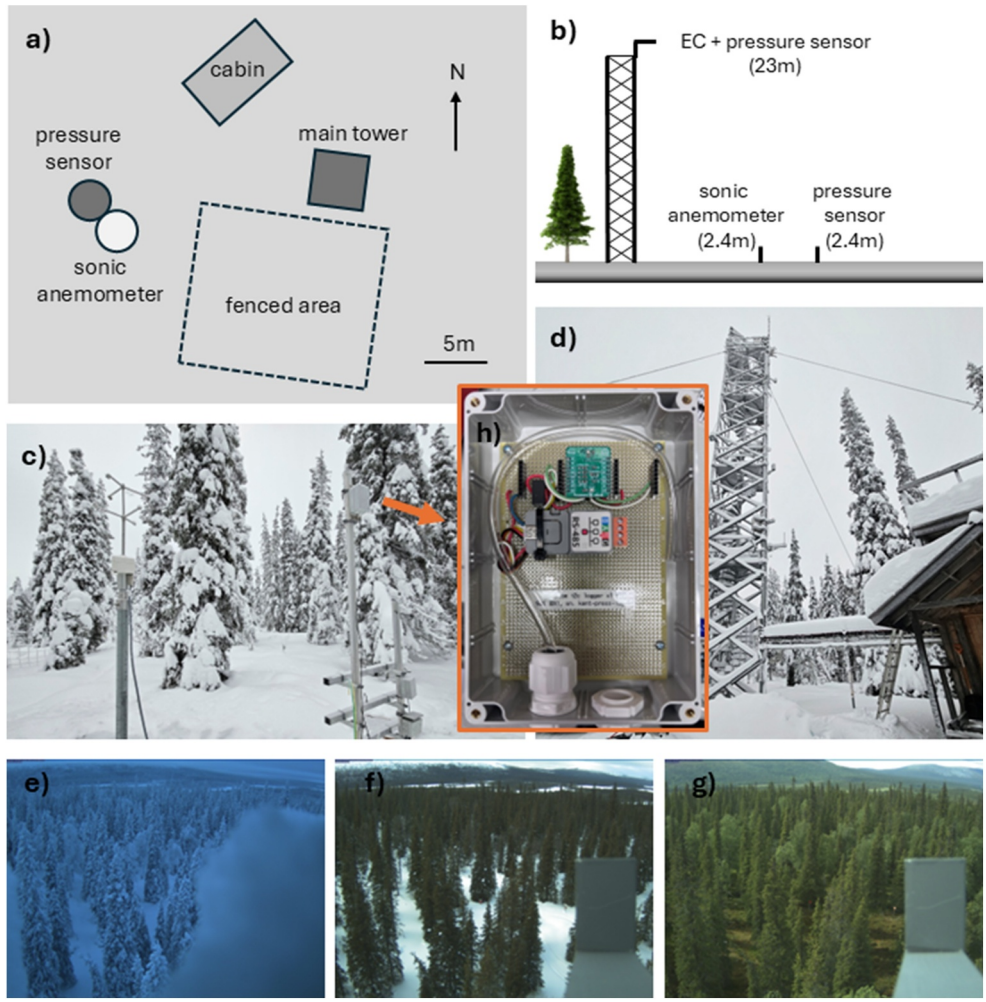

Figure 4. (a) Aerial sketch of the instrument location showing the horizontal-spatial orientation of the infrastructure and instruments. (b) Illustration of the vertical orientation of the instrumentation with respect to the average vegetation height. (c, d) show the instruments at the forest floor and the main tower, respectively. (e–g) pictures of the study site taken above the canopy at 12:30 EET with the same angle showing the three snow-cover cases investigated, that is, *all snow*, *ground snow,* and *snow-free*, respectively. (h) Interior picture of mounting enclosure where BMP581 sensor is located.

related to temperature dependency of pressure fluctuations are presented in Appendix A. All in all, good agreement in terms of correlation coefficient and one-to-one response is noted, but some finite intercept values that cannot be explained by mean air temperature or wind speed also emerged. The filtered pressure fluctuations standard deviation are compared to the standard deviation of the temperature fluctuations, but no correlation between the filtered pressure standard deviation and the temperature standard deviation appeared (see Appendix A) despite the fact that the air temperature variance follows expectations from Monin-Obukhov similarity theory for near-neutral conditions (Monin & Obukhov, 1954). To assess whether measured pressure fluctuations in the enclosure can be explained by the background instantaneous turbulent kinetic energy, a correlation analysis was conducted and presented in Appendix A. From this analysis and for almost all the 30-min runs considered, the coefficient of determination between the 10 Hz measured turbulent kinetic energy and measured p' was small and below 0.1.

All instruments were sampled at 10 Hz and the raw data were stored for later post-processing. To prevent possible distortion by the tower-fence-shed infrastructure (Figure 4a), only the data from 180–360° wind sector were used. When computing spectra from time series, Taylor's frozen turbulence hypothesis is used (Taylor, 1938; Wyngaard & Clifford, 1977). Recent wind tunnel experiments compared velocity spectra (longitudinal and vertical) obtained

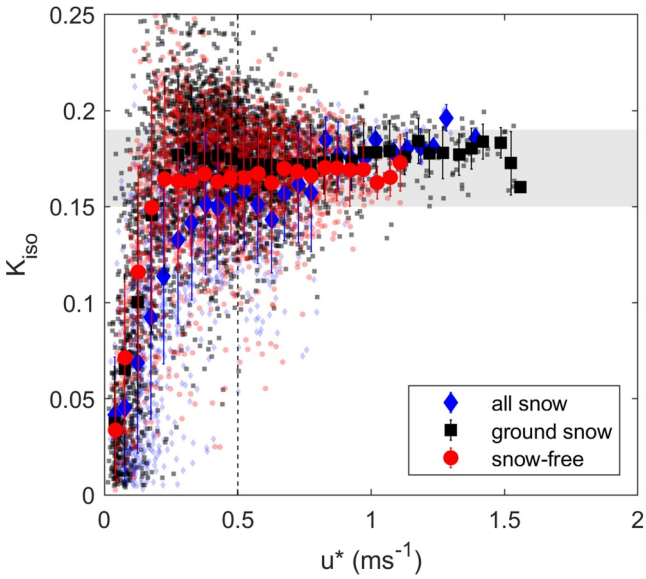

Figure 5. The variation of energy anisotropy ratio K_{iso}) with friction velocity (u_*) above the canopy for different snow cover cases, that is, *all snow*, *ground snow,* and *snow-free*. Half-hourly values are shown with small and semi-transparent markers, while the binned values are featured with big markers for the corresponding color and shape indicated in the legend. The shaded area shows the saturation range, while vertical-dashed line marks the threshold $u_* = 0.5$ ms^{-1}.

by means of a particle imaging velocimeter (PIV) and cross probe at very high Reynolds numbers. The PIV velocity spectra (space-time) did not utilize Taylor's hypothesis, whereas the cross-probe measurements in time did. The agreement between the two spectra along k_x was exceptionally high for scales up to 6δ (Deshpande et al., 2023). Hence, Taylor's hypothesis will be used without any modifications. All spectra are computed using Welch Periodogram method with a Hamming window approach.

4. Results and Discussion

To evaluate the predicted $E_{pp}(k_x)$, the results and discussion are structured as follows: The selection of the turbulence runs based on anisotropy in energy among velocity components is introduced to determine appropriate u_* classes for each of the three snow-cover periods. Next, relations between σ_p and u_*^2 are used to estimate C_p for classes in which the anisotropy measure no longer varies with u_* (similar to canonical turbulent boundary layers). Using this C_p, predictions of $E_{pp}(k_x)$ are compared with the measurements when C_{p1} is computed from the aforementioned C_p^2.

4.1. Turbulence Anisotropy in Eddy Energetics

Because stratification impacts the energy distribution in eddies, a metric is needed to assess how far turbulence is from its "canonical state" in terms of energy anisotropy. There are multiple measures that can be used such as the stability parameter or the flux Richardson number. Here, we use a different metric that is sensitive to the energy distribution in eddies—labeled as the energy anisotropy. It is given by

$$K_{iso} = \frac{\sigma_w^2}{\sigma_u^2 + \sigma_v^2 + \sigma_w^2} = \frac{1}{1 + (\sigma_u^2 + \sigma_v^2)/\sigma_w^2}, \tag{27}$$

where σ_u, σ_v, and σ_w are the root-mean-squared values of the longitudinal, lateral, and vertical turbulent velocity components, respectively. When $K_{iso} \to 0$, it implies that the turbulent kinetic energy is concentrated in u and v—and the eddies are "energetically" pan-cake like. Likewise, when $K_{iso} = 1/3$, it implies that the turbulent kinetic energy is equally partitioned among the three velocity components (isotropic). In the near-neutral ASL flows, $\sigma_u = A_u u_*$, $\sigma_v = A_v u_*$, and $\sigma_w = A_w u_*$ (Kaimal & Finnigan, 1994) so that

$$K_{iso} = \frac{1}{1 + (A_u^2 + A_v^2)/A_w^2}. \tag{28}$$

Typical values for these similarity constants are $A_u = 2.2$, $A_v = 1.9$, and $A_w = 1.25$ (Kaimal & Finnigan, 1994; Stull, 2012). Hence, $K_{iso} = 0.16$ represents a reference value for a neutrally stratified ASL. This value is roughly between 2-D turbulence ($K_{iso} = 0$) and 3-D isotropic turbulence ($K_{iso} = 0.33$). When the turbulence is strongly stably stratified, much of the turbulent energy resides in the u and v components. Stable stratification acts as a sink for the vertical velocity kinetic energy and the only source of kinetic energy is the pressure-redistribution term (the Robin Hood effect). These 2-D turbulence conditions are commonly associated with meandering that dominates eddy movements with little energy in the vertical component. As u_* increases, the K_{iso} will increase until a "saturation" value commensurate with $K_{iso} = 0.16$ is reached. That is, a critical u_* needs to be exceeded before turbulence begins to approach its 3-D "canonical" state of a neutrally stratified ASL. For those high u_* conditions, the $E_{pp}(k)$ may also attain its canonical shape for boundary layers (i.e., Figure 1) unless large meso-scale motion disrupts its onset. Such meso-scale motion is to be spectrally filtered out here when the focus is on turbulence pressure spectra.

Figure 5 shows the relation between K_{iso} and u_* for the three snow cover cases. The K_{iso} increases as u_* increases for low u_* values and reaches a plateau within the range of 0.15–0.18 as expected. Interestingly, the critical u_* is

attained differently for the three snow cover cases. For the snow free case, the critical u_* is closer to 0.2 ms^{-1}, whereas for the all snow cover, the critical u_* exceeds 0.4 ms^{-1}. The canopy roughness is certainly impacted by the presence or absence of snow on the trees as shown in Figure 4. When snow covers the trees, the crown diameter becomes more slender and the canopy appears more open. For snow-free conditions, the overall crown diameter expands, and the forested canopy appears more closed. Thus, for the snow-covered trees, the air flow within the vegetation experiences a smoother array of slender obstructions. This has two inter-related effects: the first is that any vortex shedding or wake diffusion persisting above the canopy will maintain its coherency over greater distances before encountering another obstacle. The second is that a sparser canopy may prevent a strong inflection point in the mean velocity profile and thus the formation of Kelvin-Helmholtz (KH) instabilities (i.e., mixing layer eddies) may be less frequent. The KH instabilities are quite efficient at enhancing vertical mixing near the canopy-atmosphere interface. Thus, higher u_* is required to dissipate coherent two-dimensional wake effects for the snow-covered trees. For the snow free vegetation, the crowns are wider and thus tightly spaced, the obstructions are rougher and include multiple scales. These multiple roughness scales are efficient at breaking up or, at least, randomizing any persistent two-dimensional vortices from wakes and enhances the redistribution of turbulent kinetic energy among velocity components. In short, the presence or absence of snow on the vegetation dictates how K_{iso} approaches the threshold u_* rapidly (no snow) or slowly (with snow). However, the overall saturation K_{iso} value is not appreciably impacted by snow cover (at least for $z/h = 1.64$).

Beyond using K_{iso} for canonical turbulent flows, estimates of ϵ using Equation 5 are also indirectly explored. The mean velocity gradient was not measured at $z/h = 1.67$ but a balance between turbulent kinetic energy production and dissipation allows for an estimate of the mixing length and subsequently a zero-plane displacement assuming attached eddies dominate momentum transfer. The ϵ was determined from the inertial subrange spectra of the longitudinal velocity. From Appendix B, it is shown that l_m computed from u_*^3/ϵ agree with $\kappa(z - d)$ for d/h around 0.5–0.6. The higher d/h value is for snow-free conditions where the canopy appears rougher and the crown diameter wider.

4.2. The Pressure Spectra

Figure 6 shows a sample time series of the measured static pressure variations and longitudinal velocity fluctuations (Figures 6a and 6b), their filtered version (Figures 6c and 6d), and the computed power spectra of the filtered versions (Figures 6e and 6f) for a 30 min period collected on 15 Dec. 2023 at 09:00 when u_* was 0.52 ms^{-1}. As expected, the 5 min filtering removes low-frequency modulations on time scales of about 1,000 s from the raw pressure time series. The effects of such 5 min filtering appear not as appreciable in the longitudinal velocity time series compared to its static pressure fluctuations counterpart.

The agreement between predicted and measured $E_{pp}(k_x)$ (after filtering) appears superior to its longitudinal velocity counterpart (i.e., $E_{uu}(k_x)$) when setting $\beta = 2$. The overlap region $k_x \in [1/(\beta z), 1/\delta]$ featured here is routinely used to justify the extent of a k_x^{-1} power law in $E_{uu}(k_x)$. Prior studies do suggest that β can vary with the stability parameter for velocity spectra (Huang & Katul, 2022). At the high-frequency end, the instrument noise level (flat part of the measured spectrum) dominates beyond $k_x z > 10$. The reported minimum sensor noise variance by the manufacturer is also shown as a dot-dashed line. It is clear that the actual noise is higher. Despite the higher noise level found here, there is still an appreciable signal-to-noise ratio in the measured $E_{pp}(k_x)$ where k_x^{-1} and a $k_x^{-7/3}$ are resolved across wide ranging k_x values (>2 decades).

The value of β (i.e., transition from k_x^{-1} to $k_x^{-7/3}$) was further explored in Figure 7 for different snow cover ranges. This figure presents 30 measured $E_{pp}(k_x)$ for each of the three snow cover periods when K_{iso} attained independence from u_* (>0.5 ms^{-1}). Because the focus is on whether β is impacted by the snow cover, each of the 30 pressure time series was first spectrally filtered, and then normalized to have a zero-mean and a unit variance. By and large, the k_x^{-1} and the $k_x^{-7/3}$ remain reasonable descriptors of the scaling laws. A $\beta = 2$ also appears plausible for all snow cover cases though the spectral transition region from one scaling regime to another is not as sharp (i.e., smoother than a single break-point in wavenumber space). The effects of these modest deviations from the anticipated scaling laws and transition point (i.e., $\beta = 2$) on C_p (i.e., sensitive to the area under the spectrum) is considered next.

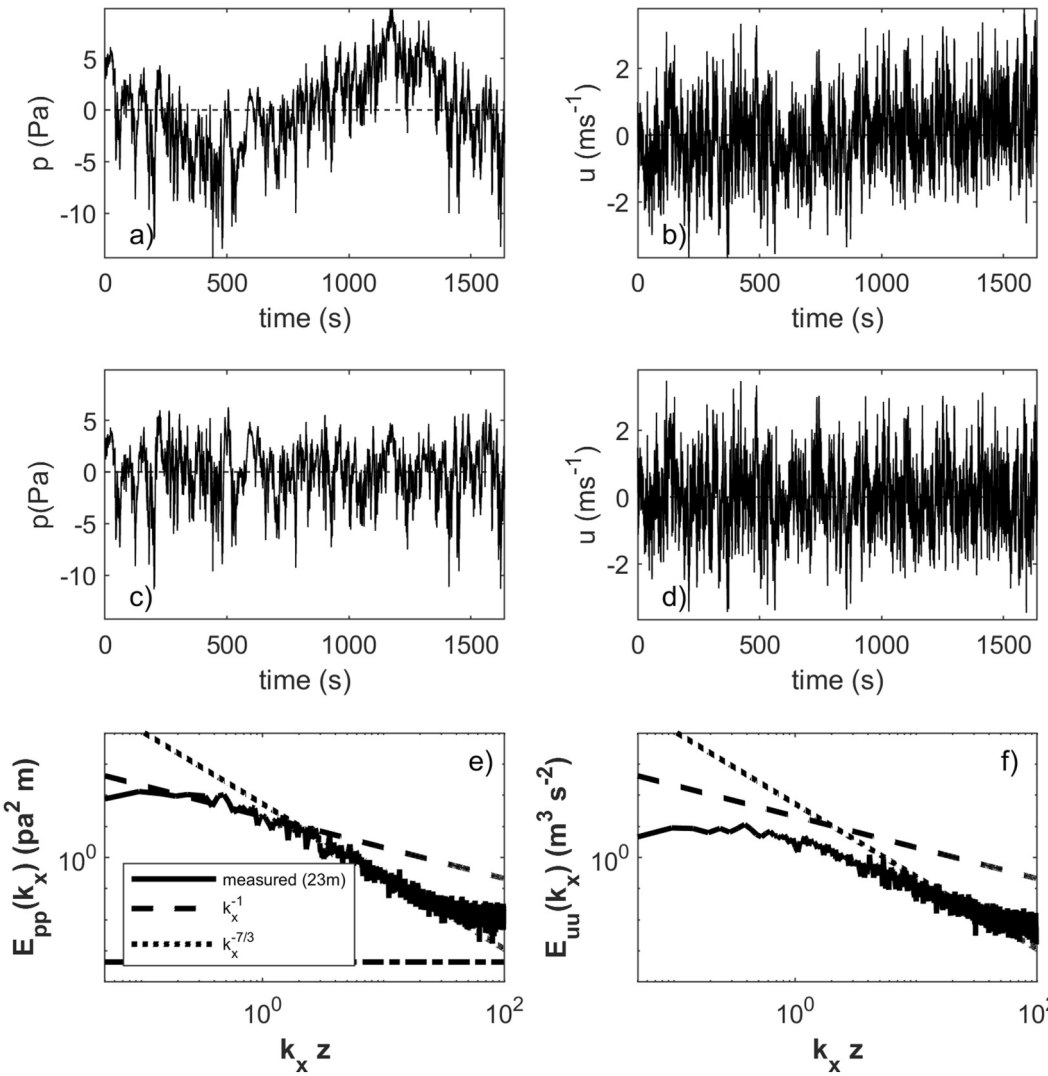

Figure 6. Measured pressure (a) and longitudinal velocity (b) series sampled at 10 Hz and de-meaned for $z = 23$ m. The data displayed were collected on 15 Dec. 2023 at 9:00 a.m. Filtered pressure (c) and filtered longitudinal velocity (d) series using a 5 min spectral cut-off are shown. Comparison between measured and predicted pressure spectra ($E_{pp}(k_x)$) for the low wavenumber regime by Equation 18 and the inertial subrange regime by Equation 14 when setting $\beta = 2$ and $A_\delta = 0.2$ (its accepted value for near-neutral flows) using the filtered pressure series (e). The k_x^{-1} power-law scaling in $E_{pp}(k_x)$ is more evident and broader across scales than its longitudinal velocity (i.e., $E_{uu}(k_x)$) counterpart (f). The dot-dashed horizontal line in the $E_{pp}(k_x)$ panel is the reported minimum sensor noise variance ($=0.08^2 \times \left[\overline{U}dt/(2\pi)\right]$ Pa^2 m).

4.3. The Normalized Pressure Variances

The relation between σ_p^2 and u_*^4 is commonly used in the literature to infer C_p^2. This relation and the empirically inferred C_p from it are now investigated for the case where K_{iso} attained a near-constant value. By regressing measured σ_p^2 (after the 5-min high-pass spectral filtering) against measured u_*^4, "effective" values for C_p^2 converged on ca. 53, as shown in Figure 8 (or C_p converged on ca. 7.3), irrespective of the snow cover. These effective values are compared to those determined from Equation 26 when varying $A_\delta = 0.1$–0.3 and $\beta = 1.5$–3 and using the C_p outcomes only for $u_* > 0.5$ ms^{-1} (or $u_*^4 > 0.0625$), as shown in Figure 9. For this u_* threshold, K_{iso} is constant and the modeled C_p from the log-scaling result varied depending on the range of u_* interrogated for the periods corresponding to the snow cover case. Figure 8, which reports only median C_p for all the u_* cases interrogated, reveals a number of dynamically interesting features about C_p. When setting A_δ to a fixed value—say $A_\delta = 0.2$, the required β that matches the empirical C_p is ca. $\beta = 2$ regardless of snow conditions.

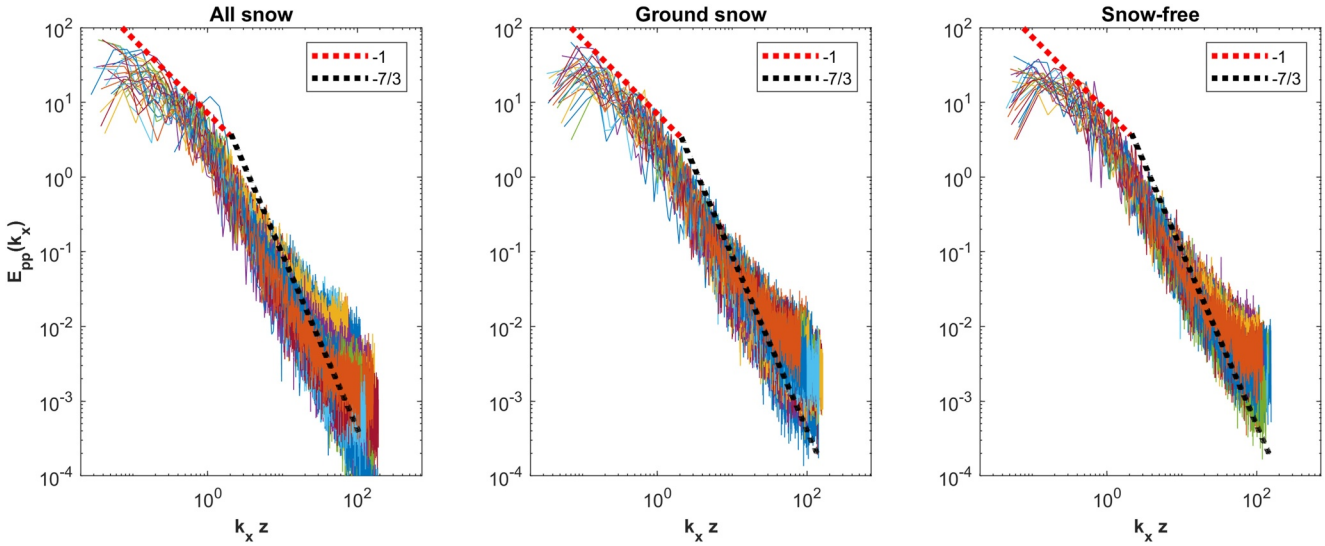

Figure 7. Measured above canopy pressure spectra of 30 half-hour periods ($E_{pp}(k_x)$) normalized by their respective variances for all three snow cover cases. Note the normalized transition wavenumber from k_x^{-1} to $k_x^{-7/3}$ for different snow cover is shown for $k_x z = \beta = 2$ as reference.

While the agreement between effective and modeled C_p is acceptable, there are a number of issues that should be raised as cautionary notes. The effective C_p inferred from the data is impacted by (a) the white-noise at high frequency in the measurements as evidenced from Figure 7, (b) a spectral exponent decaying not as steep as $k_x^{-7/3}$ in some runs (due to intermittency effects), and (c) low-frequency modulations at scales where $k_x\delta < 1$. All these effects, which are visible in several sample runs shown in Figure 7, act to increase the measured C_p in the data. On the other hand, the modeled C_p in Equation 26 does account for large-scale turbulent motion associated with the k_x^2 scaling regime. The latter scaling regime is not fully resolved by the $E_{pp}(k_x)$ measurements.

4.4. The Sub-Canopy Pressure Variances and Spectra

As a bridge to the topics raised in the introduction, the 5 min spectrally filtered pressure variances at $z = 2.4$ m were also computed and compared with their counterpart near the canopy top in Figure 10 for all three snow cover cases. As expected, the canopy filters out pressure fluctuations depending on snow conditions. The overall pressure variance near the forest floor is ca. 27% of its value at the canopy top for *all snow*, which gradually decrease to 20% for *ground snow* and further to 16% for *snow-free* conditions. The linear relation between variances found here implies that models that seek to quantify pressure pumping in snow or forest floor due to

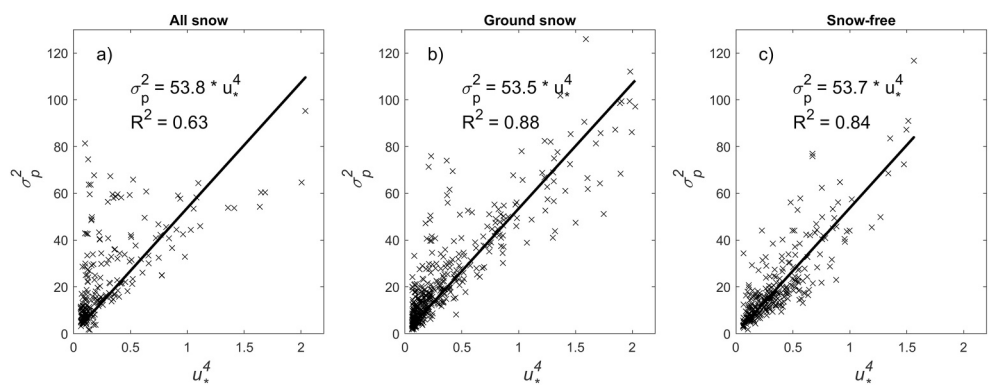

Figure 8. Relation between measured u_*^4 and σ_p^2 of the filtered pressure series above the canopy for the three different snow cover cases. The regression slope is conventionally interpreted as an effective C_p^2. The goodness of the fit is evaluated using the coefficient of determination R^2.

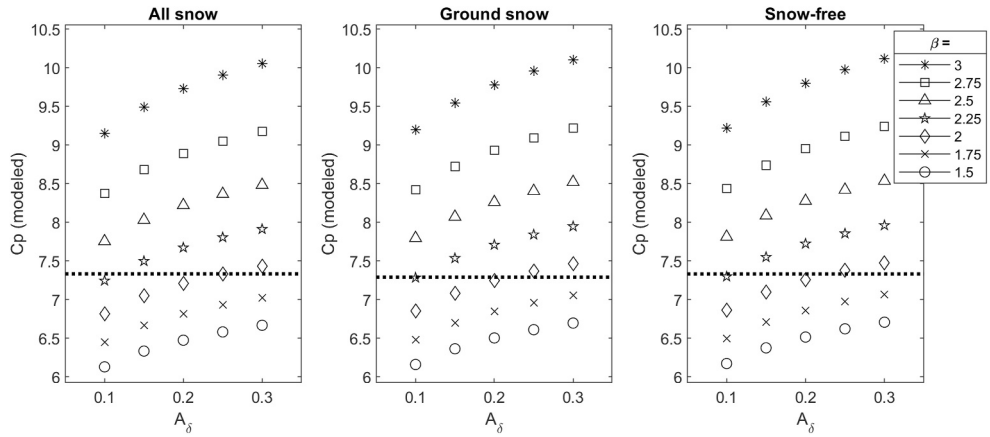

Figure 9. A comparison between estimated effective C_p from data for different snow cover cases reported in Figure 8 and modeled C_p using Equation 25. The C_p is computed for each measured u_* for typical A_δ values (0.1–0.3) and for varying β values (1.5–3). The median C_p value of each A_δ and β combination is shown with markers and estimated effective C_p from data with dotted line (ca. 7.3 for all snow cases).

turbulence can use the scaling laws for $E_{pp}(k_x)$ above the canopy and the variance reduction derived here. In fact, Figure 11 confirms that the same scaling laws as those reported near the canopy top reasonably describe the normalized pressure spectra at $z = 2.4$ m further confirming this conjecture. Thus, it appears that the canopy here, and for all snow conditions, is simply removing pressure variance in proportion to the squared amplitude associated with each scale with no preferential scale cut-off. The β value separating the transition from k_x^{-1} to $k_x^{-7/3}$ regime is also around $\beta = 2$. This similarity in scaling laws should be accompanied with cautionary notes including the use of Taylor's frozen turbulence hypothesis where much higher turbulent intensity in the sub-canopy space is encountered. Also, even small local topographic variations (compared with h) can impact the static pressure spectra near the snow top.

5. Conclusion and Future Outlook

The spectral properties of the turbulent static pressure fluctuations $E_{pp}(k_x)$ were analyzed above a subarctic forest canopy for near neutral conditions across a wide range of snow cover. The work demonstrated the following:

1. The critical friction velocity (u_*) beyond which the turbulent kinetic energy partition among velocity components is reasonably approximated by standard near-neutral surface layer similarity is sensitive to the snow cover conditions. Much higher u_* values are needed when trees are covered with snow (>0.5 ms^{-1}) compared to snow-free ecosystem (>0.2 ms^{-1}). The remaining conclusions apply for u_* values exceeding these thresholds.

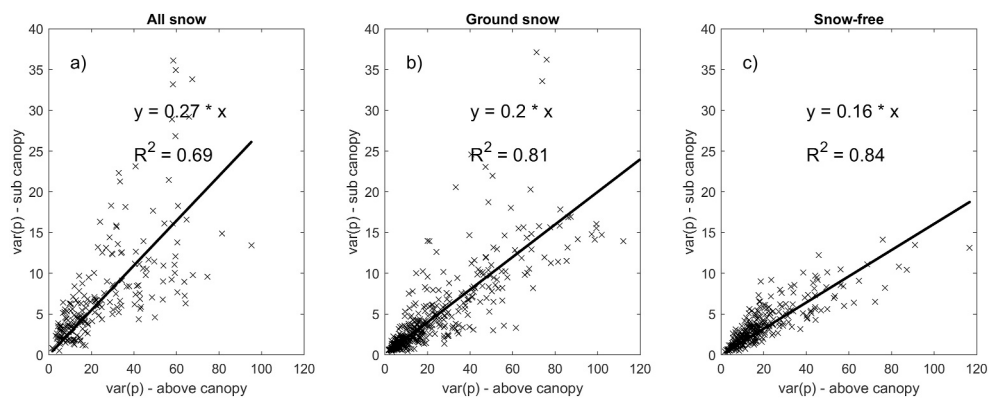

Figure 10. Relation between measured pressure variances above ($z = 23$ m) and below the canopy ($z = 2.4$ m) of the filtered series for the three different snow cover cases.

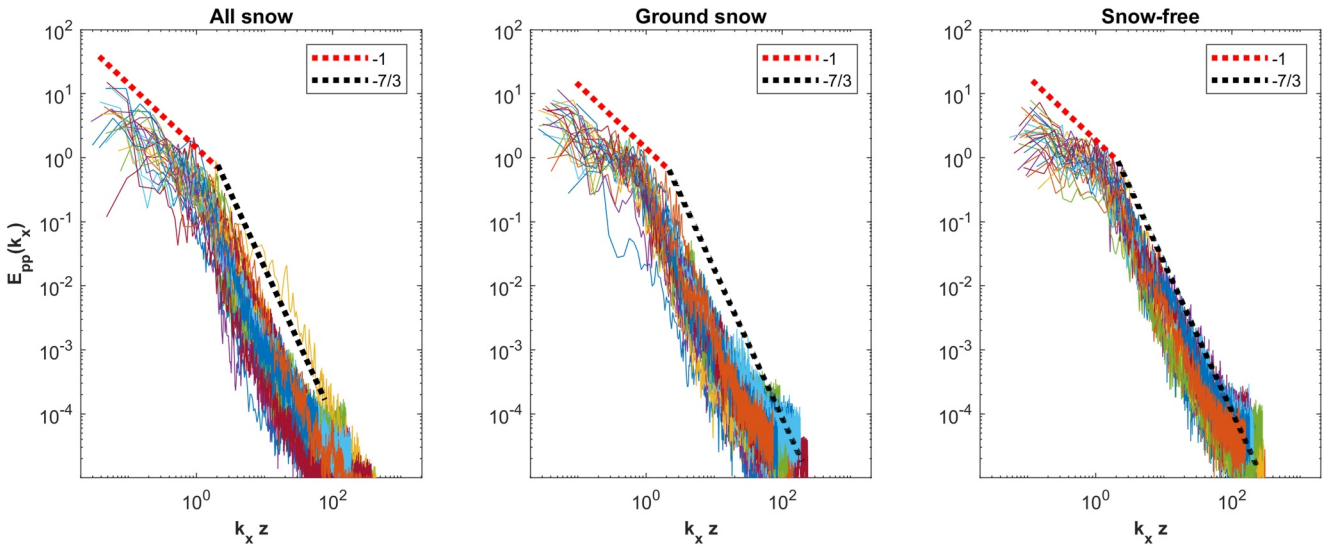

Figure 11. Measured subcanopy pressure spectra of 30 half-hour periods ($E_{pp}(k_x)$) normalized by their respective variances for all three snow cover cases.

2. For the inertial subrange in which $k_x z > \beta$, the $E_{pp}(k_x)$ is approximated by $C_{p1}\epsilon^{4/3}k_x^{-7/3}$, where $\beta = 2$ (derived from measurements) and $C_{p1} = 8$, the latter constant is consistent with DNS.
3. For the overlap region in which $k_x z < \beta$ and $k_x \delta > 1.5 - 2.5$, the $E_{pp}(k_x)$ is defined as $C_{p2}u_*^4 k_x^{-1}$, where $C_{p2} = \sigma_p^2/u_*^4$ and is not a constant. It is given by a log-linear relation in z/δ analogous to the attached eddy model for σ_u^2/u_*^2.
4. The aforementioned spectral scaling laws appear to hold in the trunk space just above the snow cover. This implies that the canopy filters out turbulent pressure variances in proportion to their squared amplitudes without any preferential selection across scales.
5. The filtered pressure variance in the sub-canopy space varies from 27% for all snow to 16% for snow free conditions when compared to the filtered pressure variance at the canopy top. While the tree density and tree height are the same for both snow cover cases, the all snow cover case makes the trees appear more slender and smoother compared to their snow free counterpart. This effect implies less pressure variance filtering in the all snow cover case.
6. The low-cost static pressure sensors employed here (BMP581, BOSCH, Germany) can resolve pressure fluctuations albeit with a small non-constant drift. Despite these limitations, the turbulence pressure spectra derived from the BMP581 sensors agree with theories and similarity coefficients explored using DNS. When compared with standard high-precision digital barometers (PTB220, Vaisala, Finland) using linear regression, the regression slope and the coefficient of determination are near unity. The intercept variations across the winter-spring season were not small and ranged from 0.2 to 1.4 kPa (discussed in Appendix). This work adds to the growing trend of exploring the use of low-cost pressure sensors to quantify spectral properties of pressure (Mayor et al., 2023).

Future experiments will include a ceilometer to estimate the boundary layer height and thus constrain the value of A_δ in near-neutral conditions for future analysis. With extended measurement campaigns, the ensemble-averaged spectra may reliably discern the transition regime from the k_x^{-1} to $k_x^{-7/3}$ and thus β. More broadly, the role of thermal stratification on the pressure spectra as well as the inclusion of such pressure spectra in numerical models for pressure pumping in snow is a topic that is better kept for a future inquiry.

Appendix A: Pressure Sensor Diagnostics

This appendix reports comparisons between the pressure sensor used in the high-frequency analysis here (BMP581) and a reference pressure sensor (PTB220 Digital Barometer, Vaisala, Finland) available at the site supporting a standard weather station. Minutely averaged BMP581 and sampled PTB220 absolute pressure

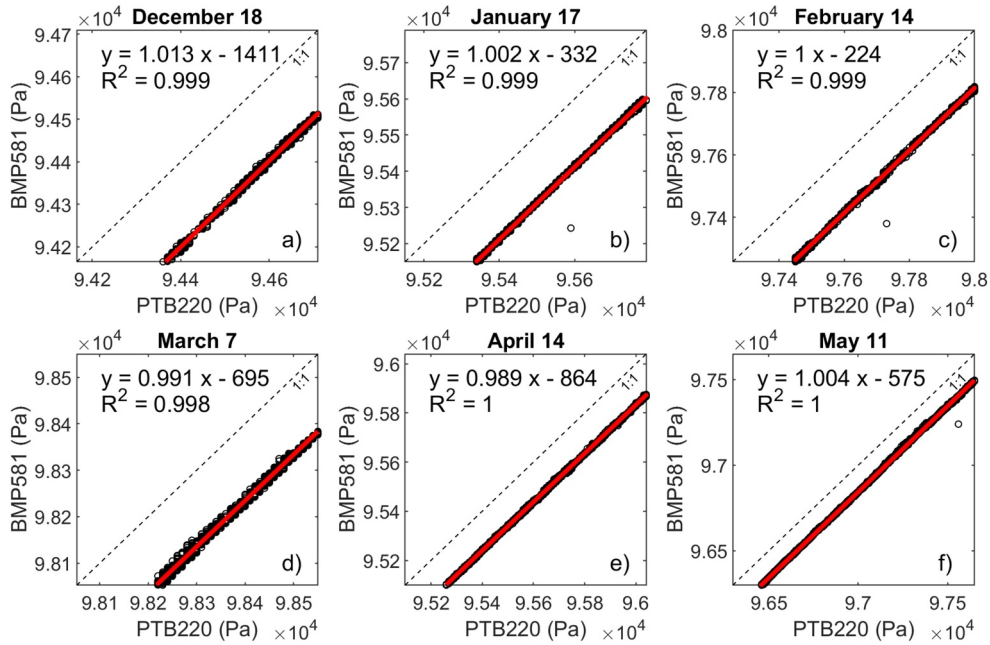

Figure A1. Comparison between Vaisala-PTB220 located at 2 m integrated in AWS and BMP581 absolute pressure sensor located at 23 m. The panels show daily variations for a chosen day in every month between Dec and May.

showed good agreement ($R^2 \sim 1$ and slope ~ 1) across months for selected days (Figure A1). Despite this agreement, varying offset between 0.2 and 1.4 kPa for different months were observed. These offsets were small in absolute when compared with the mean pressures (about 95 kPa). The manufacturer does report a temperature coefficient offset of ±0.5 Pa/K, which may explain some of the variations in the regression intercept determined in Figure A1. To further explore any $\overline{T}$ or wind speed dependency, the relation between mean $\overline{T}$ and wind speed and the associated offset values in Figure A1 was analyzed. It was found that the effect of such meteorological variables on instrument performance was not significant when absolute values were considered.

The effect of air temperature fluctuations within each 30 min run on pressure fluctuations was also considered. The mean air temperature measured at $z = 23$ m every 30 min varied between −25 and +25°C during the campaign (Figure A2a). The associated temperature variance σ_T was computed for each 30 min run and an assessment was made as to whether the air temperature variability within a given 30 min run impacts the pressure fluctuations for the same 30 min. Before computing σ_T, the number of runs experiencing spikes was first checked and found to be infrequent. When temperature spikes do occur in a given 30 min run, their numbers remained well below 50 out of 18,000 (Figure A2b). Thus, the spikes were removed and gap-filled for the purposes of computing σ_T. As noted earlier, the high-frequency pressure data were categorized with different mean air temperature classes (Figure A3) and the runs featured here interrogate all snow conditions (*all snow*, *ground snow,* and *snow-free*). The analysis to be presented next was limited to 240–300° wind sector to minimize the effect of sensor separation between sonic anemometer and pressure sensor, which were located on 160–340° axis with 2 m horizontal separation at the same height. Based on the analysis here, the σ_T of each 30 min run remained below 1°C, while filtered σ_p were below 12 Pa. The relation between σ_T and σ_p was analyzed to assess whether there are dependencies between σ_p and σ_T in any given temperature class. The findings shown in Figure A3 suggest that σ_T variability is not correlated with filtered σ_p (i.e., pressure fluctuations due to turbulence only) for each temperature class.

It is worth noting that σ_T and σ_p are jointly impacted by u_* when $|\overline{w'T'}| \geq 0.02$ m s^{-1} K. In fact, the σ_T variations here can be explained by the turbulent sensible heat and u_* using Monin-Obukhov similarity theory (Monin &

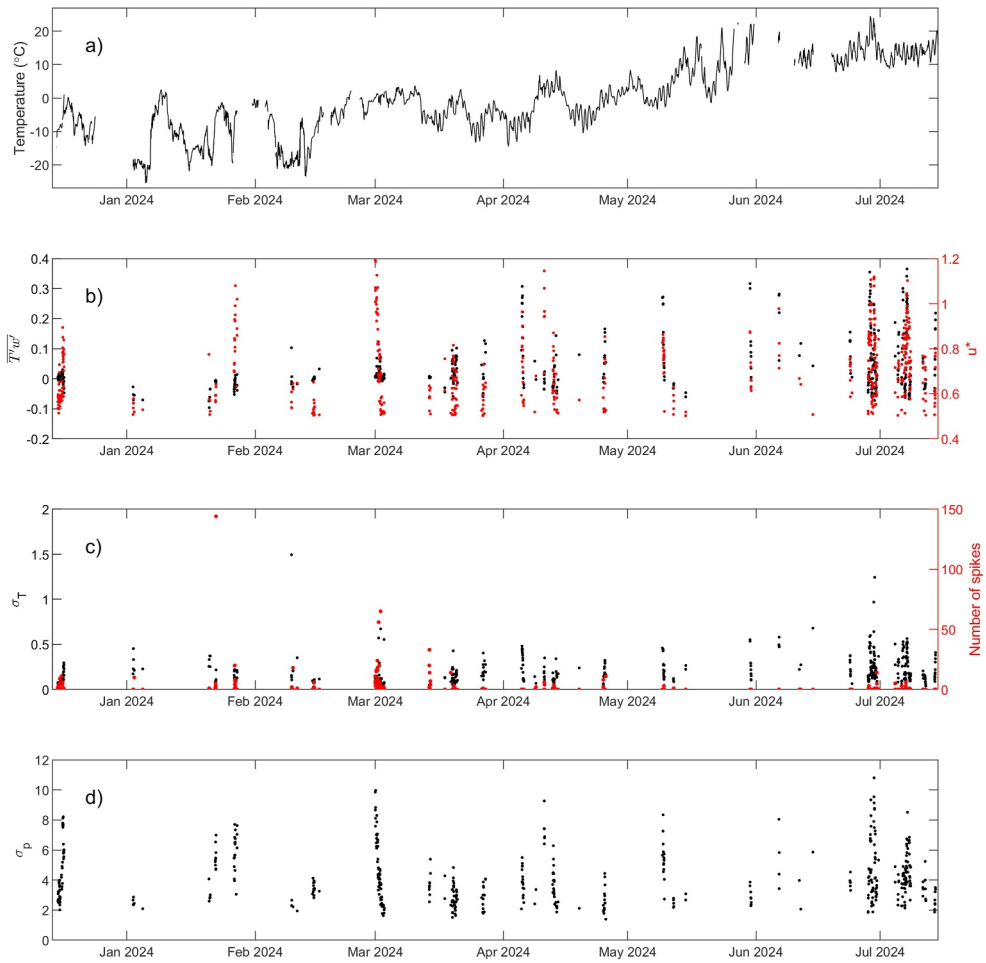

Figure A2. (a) Time series of measured air temperature at 23 m during the experiment. (b) Kinematic sensible heat flux and friction velocity. (c) Standard deviation of air temperature σ_T and the number of spikes in each half-hour period. (d) Standard deviation of filtered pressure measured at 23 m as described in Section 3.

Obukhov, 1954). Specifically, it was found that in near-neutral conditions, σ_T variations can be reasonably explained by $T_* = |\overline{w'T'}/u_*|$ as shown in Figure A4. More interesting is that the regression slope (=1.28) is commensurate to that reported in the Kansas and other experiments for near-neutral atmospheric stability conditions where $\sigma_T/T_* = \sqrt{1.8} = 1.34$ (i.e., close to 1.28) as summarized elsewhere (Sorbjan, 1989). This analysis is suggestive that measured turbulent pressure fluctuations by the BMP581 sensor are unlikely to be driven by temperature fluctuations.

The relation between p' and instantaneous turbulent kinetic energy $e(t) = (1/2)\left(u'(t)^2 + v'(t)^2 + w'(t)^2\right)$ was also considered to assess whether the dynamic pressure fluctuations played a significant role on the measured p' within the enclosure (Figure A5). Here, $e(t)$ was selected because it is a scalar and reflects the intensity of the turbulence in the vicinity of the boxed pressure sensor. Figure A5 suggests that for the 30-min runs analyzed here, the coefficient of determination between $p'(t)$ (filtered and raw) and $e(t)$ was small in almost all cases. That is, if the dynamic pressure head is assumed to be related to the background $e(t)$, the analysis here seems to suggest that the dynamic contribution is not significant.

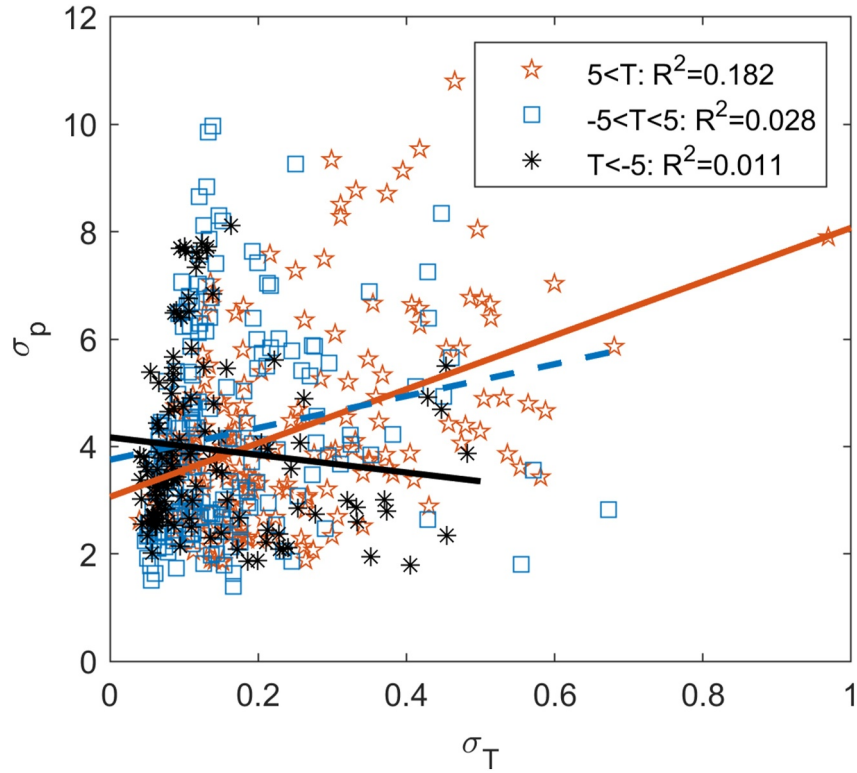

Figure A3. Relation between standard deviation of temperature as measured using the sonic anemometer (σ_T) and the standard deviation of the filtered pressure fluctuations (σ_p) for different mean air temperature classes. The fitted lines are shown with corresponding colors, while the goodness of fit (R^2) is shown for each classes next to the legend. Both σ_T and σ_p are impacted by u_*.

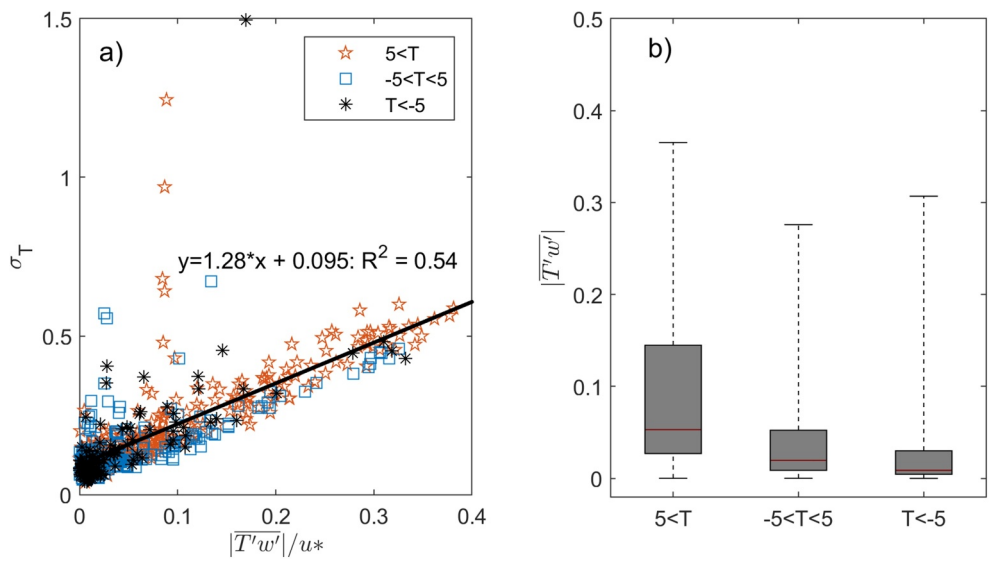

Figure A4. (a) The relation between the absolute kinematic heat flux $|\overline{w'T'}|$ normalized with friction velocity u_* (abscissa) against the standard deviation of temperature (ordinate) for each mean air temperature class and $u_* \geq 0.5$ m s^{-1}. A constant slope is suggestive that σ_T is explained by $T_* = |\overline{w'T'}/u_*|$ as predicted from Monin and Obukhov (1954) similarity theory. (b) The variation of the absolute kinematic heat flux $|\overline{w'T'}|$ for each mean air temperature class is also shown for reference.

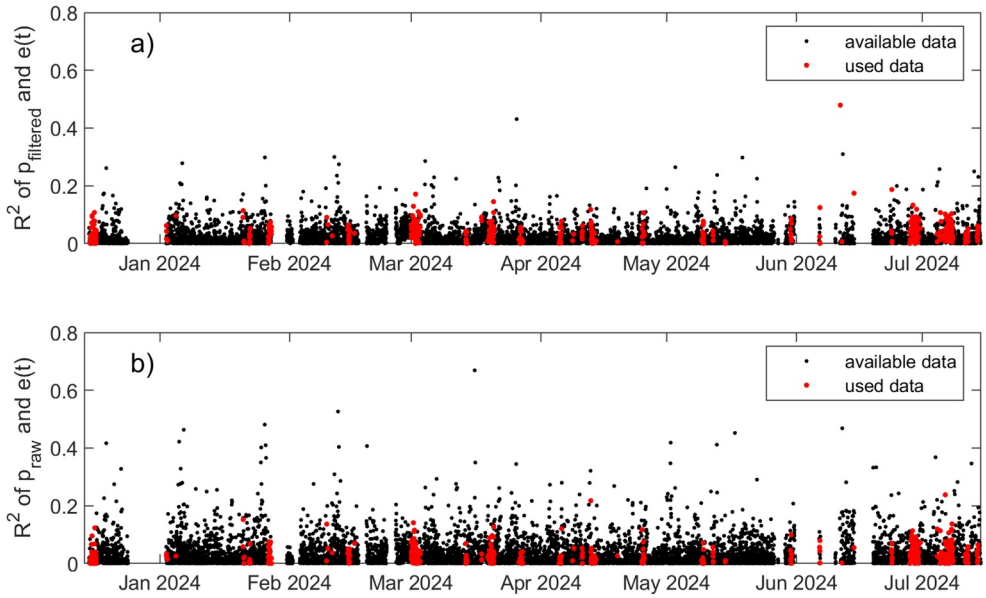

Figure A5. The goodness of fit (R^2) of filtered ($p_{filtered}$) and raw (p_{raw}) pressure perturbations and fluctuating turbulent kinetic energy (e(t)).

Appendix B: Production to Dissipation Balance

The relation between $\epsilon(z)$ and u_*^3/l_m above the canopy at $z/h = 1.64$ is explored in Figure B1. The interest in $l_m(z) = u_*^3/\epsilon(z)$ has received significant attention in canopy turbulence and surface layer scaling analysis (Chamecki et al., 2017; Davidson & Krogstad, 2014; Ghannam et al., 2018; Mortarini et al., 2023) as it allows for some deviations from the law-of-the wall to be accommodated due to imbalances between turbulent kinetic energy production and its dissipation. For the attached eddy hypothesis, l_m is determined from eddies attached to the zero-plane displacement d. Thus, to infer l_m, the measured longitudinal velocity spectra $E_{uu}(k_x)$ are used. For $k_x z > 2$, the $E_{uu}(k_x)$ spectra are approximated by their inertial subrange form given by

$$E_{uu}(k_x) = C_{o,u}\epsilon^{2/3}k_x^{-5/3}, \tag{B1}$$

where $C_{o,u} = 0.5$ is the Kolmogorov constant (Kaimal & Finnigan, 1994). For the runs used here (i.e., $u_* \geq 0.5$ m s^{-1}), the estimates of ϵ were determined by regressing $\log[E_{uu}(k_x)]$ upon $\log(k_x)$ for eddy sizes within the inertial subrange. The resulting spectral exponents varied from -1.5 to -1.67, as shown in Figure B1a. The regression intercepts were then used to infer ϵ. Once ϵ was determined for a given run, the associated u_*^3 was computed. An overall regression analysis was then conducted with u_*^3 as the dependent variable and ϵ as the independent variable for all three temperature classes (Figure B1b). The slope of this regression can then be interpreted as l_m to be compared to $\kappa(z - \alpha h)$ (i.e., $d = \alpha h$). For dense canopies, textbook values suggest $d/h = 2/3$ (Kaimal & Finnigan, 1994). For sparse canopies, the α values can be much lower (Kunadi et al., 2024). When using $\kappa = 0.4$, $z = 23$ m, the α values were then computed for each air temperature range (roughly coincident with snow cover) using

$$\alpha = \frac{d}{h} = \frac{z}{h} - \frac{l_m}{\kappa h}. \tag{B2}$$

For l_m about 6.36 as determined from the robust regression analysis in Figure B1b, α is around 0.51 (<0.67), which may be plausible as the canopy may appear sparser for this temperature range due to the presence of snow on the vegetation. For l_m about 5.78, α is around 0.6, which is close to expectations for dense canopies. That $\alpha = 0.6$ and is close to $2/3$ as derived from a balance between production and dissipation of turbulent kinetic

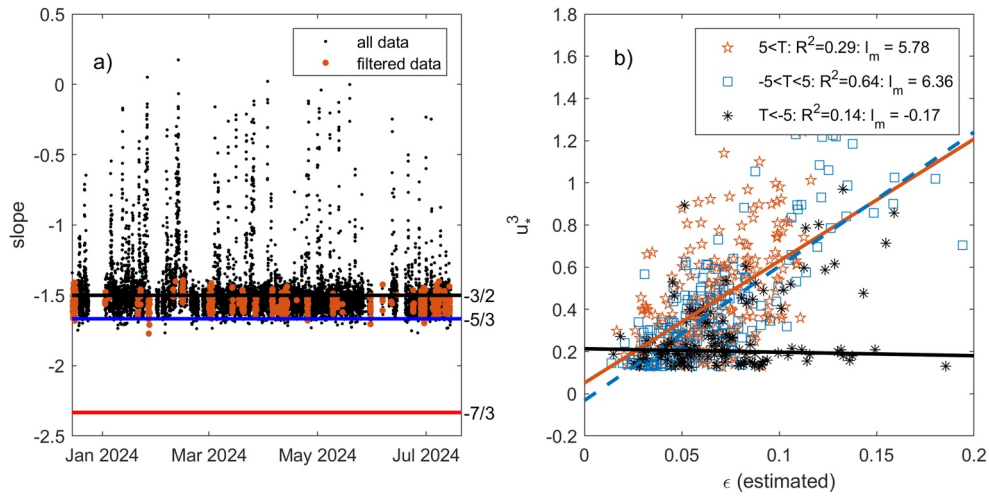

Figure B1. (a) The spectral decay rates obtained from measured $E_{uu}(k_x)$ via linear regression in logarithmic scale within inertial subrange. Black dots indicate all measured data while red dots show the filtered ones used in the analysis. The horizontal lines are inertial subrange spectral exponents corresponding to −3/2, −5/3, and −7/3. (b) The relation between the dissipation rate ϵ estimated from measured $E_{uu}(k_x)$ against measured u_*^3 for three different temperature classes. For each temperature class, the goodness of fit (R^2) and the regression slope are featured. The regression slopes are used to compute the effective mixing length l_m that can be compared with $\kappa(z - d)$. The regression slopes are determined from a robust fit that filters outliers (i.e., *robustfit* in Matlab, Mathworks, MA, USA).

energy is suggestive that this balance holds for $z/h = 1.67$. For air temperature values well below freezing, a much poorer correlation between ϵ and u_*^3 was obtained. We do not have a definitive explanation as to why.

Data Availability Statement

Data to reproduce the figures in the main text are available in Aslan et al. (2025).

Acknowledgments

GK acknowledges support from the US National Science Foundation (NSF-AGS-2028633) and the US Department of Energy (DE-SC0022072). TA and MA acknowledges the support from the Research Council of Finland (no. 347780 (ForClimate), 347860 (C-NEUT), 347664 (CWI)). TA also acknowledges support via STSM grant from COST Action CLEANFOREST (CA21138), supported by COST (European Cooperation in Science and Technology). Juha Hatakka, Juuso Rainne, and Sami Suopajärvi are acknowledged for building the measurement setup and maintaining the data flow.

References

Albertson, J. D., Katul, G. G., Parlange, M. B., & Eichinger, W. E. (1998). Spectral scaling of static pressure fluctuations in the atmospheric surface layer: The interaction between large and small scales. *Physics of Fluids*, *10*(7), 1725–1732. https://doi.org/10.1063/1.869689

Alvelius, K., & Johansson, A. (2000). LES computations and comparison with Kolmogorov theory for two-point pressure–velocity correlations and structure functions for globally anisotropic turbulence. *Journal of Fluid Mechanics*, *403*, 23–36. https://doi.org/10.1017/s0022112099006862

Arya, S. (1981). Parameterizing the height of the stable atmospheric boundary layer. *Journal of Applied Meteorology and Climatology*, *20*(10), 1192–1202. https://doi.org/10.1175/1520-0450(1981)020<1192:pthots>2.0.co;2

Aslan, T., Katul, G., & Aurela, M. (2025). The turbulent pressure spectrum within the roughness sublayer of a subarctic forest canopy [Dataset]. *Zenodo*. https://doi.org/10.5281/zenodo.14747970

Aurela, M., Lohila, A., Tuovinen, J.-P., Hatakka, J., Penttilä, T., & Laurila, T. (2015). Carbon dioxide and energy flux measurements in four northern-boreal ecosystems at Pallas. *Boreal Environment Research*, *14*, 699–710.

Banerjee, T., & Katul, G. (2013). Logarithmic scaling in the longitudinal velocity variance explained by a spectral budget. *Physics of Fluids*, *25*(12). https://doi.org/10.1063/1.4837876

Batchelor, G. K. (1951). Pressure fluctuations in isotropic turbulence. *Mathematical Proceedings of the Cambridge Philosophical Society*, *47*(2), 359–374. https://doi.org/10.1017/s0305004100026712

Blake, W. K. (1970). Turbulent boundary-layer wall-pressure fluctuations on smooth and rough walls. *Journal of Fluid Mechanics*, *44*(4), 637–660. https://doi.org/10.1017/s0022112070002069

Boano, F., Harvey, J. W., Marion, A., Packman, A. I., Revelli, R., Ridolfi, L., & Wörman, A. (2014). Hyporheic flow and transport processes: Mechanisms, models, and biogeochemical implications. *Reviews of Geophysics*, *52*(4), 603–679. https://doi.org/10.1002/2012rg000417

Boffetta, G., Mazzino, A., Musacchio, S., & Vozella, L. (2009). Kolmogorov scaling and intermittency in Rayleigh-Taylor turbulence. *Physical Review E*, *79*(6), 065301. https://doi.org/10.1103/physreve.79.065301

Boulton, A. J., Findlay, S., Marmonier, P., Stanley, E. H., & Valett, H. M. (1998). The functional significance of the hyporheic zone in streams and rivers. *Annual Review of Ecology and Systematics*, *29*(1), 59–81. https://doi.org/10.1146/annurev.ecolsys.29.1.59

Bowling, D., & Massman, W. (2011). Persistent wind-induced enhancement of diffusive CO_2 transport in a mountain forest snowpack. *Journal of Geophysical Research*, *116*(G4), G04006. https://doi.org/10.1029/2011jg001722

Bradshaw, P. (1967). Inactive'motion and pressure fluctuations in turbulent boundary layers. *Journal of Fluid Mechanics*, *30*(2), 241–258. https://doi.org/10.1017/s0022112067001417

Burns, S. P., Frank, J. M., Massman, W. J., Patton, E. G., & Blanken, P. D. (2021). The effect of static pressure-wind covariance on vertical carbon dioxide exchange at a windy subalpine forest site. *Agricultural and Forest Meteorology*, *306*, 108402. https://doi.org/10.1016/j.agrformet.2021.108402

Chamecki, M., Dias, N. L., Salesky, S. T., & Pan, Y. (2017). Scaling laws for the longitudinal structure function in the atmospheric surface layer. *Journal of the Atmospheric Sciences*, *74*(4), 1127–1147. https://doi.org/10.1175/jas-d-16-0228.1

Charuchittipan, D., & Wilson, J. (2009). Turbulent kinetic energy dissipation in the surface layer. *Boundary-Layer Meteorology*, *132*(2), 193–204. https://doi.org/10.1007/s10546-009-9399-x

Clarke, R. (1970). Observational studies in the atmospheric boundary layer. *Quarterly Journal of the Royal Meteorological Society*, *96*(407), 91–114. https://doi.org/10.1002/qj.49709640709

Colbeck, S. (1989). Air movement in snow due to windpumping. *Journal of Glaciology*, *35*(120), 209–213. https://doi.org/10.3189/s0022143000004524

Corcos, G. (1964). The structure of the turbulent pressure field in boundary-layer flows. *Journal of Fluid Mechanics*, *18*(3), 353–378. https://doi.org/10.1017/s002211206400026x

Cortina, G., Calaf, M., & Cal, R. B. (2016). Distribution of mean kinetic energy around an isolated wind turbine and a characteristic wind turbine of a very large wind farm. *Physical Review Fluids*, *1*(7), 074402. https://doi.org/10.1103/physrevfluids.1.074402

Davidson, P., & Krogstad, P.-Å. (2014). A universal scaling for low-order structure functions in the log-law region of smooth-and rough-wall boundary layers. *Journal of Fluid Mechanics*, *752*, 140–156. https://doi.org/10.1017/jfm.2014.286

Deshpande, R., de Silva, C. M., & Marusic, I. (2023). Evidence that superstructures comprise self-similar coherent motions in high Reynolds number boundary layers. *Journal of Fluid Mechanics*, *969*, A10. https://doi.org/10.1017/jfm.2023.566

Ding, M., Nguyen, K. X., Liu, S., Otte, M. J., & Tong, C. (2018). Investigation of the pressure–strain-rate correlation and pressure fluctuations in convective and near neutral atmospheric surface layers. *Journal of Fluid Mechanics*, *854*, 88–120. https://doi.org/10.1017/jfm.2018.576

Elliott, J. A. (1972). Microscale pressure fluctuations measured within the lower atmospheric boundary layer. *Journal of Fluid Mechanics*, *53*(2), 351–384. https://doi.org/10.1017/s0022112072000199

Farabee, T. M., & Casarella, M. J. (1991). Spectral features of wall pressure fluctuations beneath turbulent boundary layers. *Physics of Fluids A: Fluid Dynamics*, *3*(10), 2410–2420. https://doi.org/10.1063/1.858179

Farrell, D., Greacen, E., & Gurr, C. (1966). Vapor transfer in soil due to air turbulence. *Soil Science*, *102*(5), 305–313. https://doi.org/10.1097/00010694-196611000-00005

Fritsch, D. J., Vishwanathan, V., Roy, C. J., Todd Lowe, K., & Devenport, W. J. (2023). Modeling the surface pressure spectrum on rough walls in pressure gradients. *Journal of Fluids Engineering*, *145*(12). https://doi.org/10.1115/1.4062821

George, W. K., Beuther, P. D., & Arndt, R. E. (1984). Pressure spectra in turbulent free shear flows. *Journal of Fluid Mechanics*, *148*, 155–191. https://doi.org/10.1017/s0022112084002299

Ghannam, K., Katul, G. G., Bou-Zeid, E., Gerken, T., & Chamecki, M. (2018). Scaling and similarity of the anisotropic coherent eddies in near-surface atmospheric turbulence. *Journal of the Atmospheric Sciences*, *75*(3), 943–964. https://doi.org/10.1175/jas-d-17-0246.1

Goody, M. (2004). Empirical spectral model of surface pressure fluctuations. *AIAA Journal*, *42*(9), 1788–1794. https://doi.org/10.2514/1.9433

Gotoh, T., & Fukayama, D. (2001). Pressure spectrum in homogeneous turbulence. *Physical Review Letters*, *86*(17), 3775–3778. https://doi.org/10.1103/physrevlett.86.3775

Gotoh, T., & Nakano, T. (2003). Role of pressure in turbulence. *Journal of Statistical Physics*, *113*(5/6), 855–874. https://doi.org/10.1023/a:1027316804161

Gotoh, T., & Rogallo, R. S. (1999). Intermittency and scaling of pressure at small scales in forced isotropic turbulence. *Journal of Fluid Mechanics*, *396*, 257–285. https://doi.org/10.1017/s0022112099005972

Hanjalić, K., & Launder, B. E. (1972). A Reynolds stress model of turbulence and its application to thin shear flows. *Journal of Fluid Mechanics*, *52*(4), 609–638. https://doi.org/10.1017/s002211207200268x

Heisenberg, W. (1948). Zur statistischen theorie d e r turbulenz. *Zeitschrift für Physik*, *124*(7–12), 628–657. https://doi.org/10.1007/bf01668899

Hill, R. J., & Wilczak, J. M. (1995). Pressure structure functions and spectra for locally isotropic turbulence. *Journal of Fluid Mechanics*, *296*, 247–269. https://doi.org/10.1017/s0022112095002126

Hirose, C., Ikegaya, N., & Hagishima, A. (2020). Outdoor measurements of relationship between canopy flow and wall pressure distributions of a block within urban-like block array. *Building and Environment*, *176*, 106881. https://doi.org/10.1016/j.buildenv.2020.106881

Hsieh, C.-I., & Katul, G. G. (1997). Dissipation methods, Taylor's hypothesis, and stability correction functions in the atmospheric surface layer. *Journal of Geophysical Research*, *102*(D14), 16391–16405. https://doi.org/10.1029/97jd00200

Huang, K. Y., & Katul, G. G. (2022). Profiles of high-order moments of longitudinal velocity explained by the random sweeping decorrelation hypothesis. *Physical Review Fluids*, *7*(4), 044603. https://doi.org/10.1103/physrevfluids.7.044603

Hubbard, R. M., Ryan, M. G., Elder, K., & Rhoades, C. C. (2005). Seasonal patterns in soil surface CO2 flux under snow cover in 50 and 300 year old subalpine forests. *Biogeochemistry*, *73*(1), 93–107. https://doi.org/10.1007/s10533-004-1990-0

Joseph, L. A., Molinaro, N. J., Devenport, W. J., & Meyers, T. W. (2020). Characteristics of the pressure fluctuations generated in turbulent boundary layers over rough surfaces. *Journal of Fluid Mechanics*, *883*, A3. https://doi.org/10.1017/jfm.2019.813

Kaimal, J. C., & Finnigan, J. J. (1994). *Atmospheric boundary layer flows: Their structure and measurement*. Oxford University Press.

Katul, G. G., Albertson, J. D., Parlange, M. B., Hsieh, C.-I., Conklin, P. S., Sigmon, J. T., & Knoerr, K. R. (1996). The inactive eddy motion and the large-scale turbulent pressure fluctuations in the dynamic sublayer. *Journal of the Atmospheric Sciences*, *53*(17), 2512–2524. https://doi.org/10.1175/1520-0469(1996)053<2512:tematl>2.0.co;2

Katul, G. G., Konings, A. G., & Porporato, A. (2011). Mean velocity profile in a sheared and thermally stratified atmospheric boundary layer. *Physical Review Letters*, *107*(26), 268502. https://doi.org/10.1103/physrevlett.107.268502

Katul, G. G., Porporato, A., Manes, C., & Meneveau, C. (2013). Co-spectrum and mean velocity in turbulent boundary layers. *Physics of Fluids*, *25*(9). https://doi.org/10.1063/1.4821997

Kim, J. (1989). On the structure of pressure fluctuations in simulated turbulent channel flow. *Journal of Fluid Mechanics*, *205*(-1), 421–451. https://doi.org/10.1017/s0022112089002090

Kimball, B., & Lemon, E. (1970). Spectra of air pressure fluctuations at the soil surface. *Journal of Geophysical Research*, *75*(33), 6771–6777. https://doi.org/10.1029/jc075i033p06771

Kolmogorov, A. N. (1962). A refinement of previous hypotheses concerning the local structure of turbulence in a viscous incompressible fluid at high Reynolds number. *Journal of Fluid Mechanics*, *13*(1), 82–85. https://doi.org/10.1017/s0022112062000518

Kolmogorov, A. N. (1991). The local structure of turbulence in incompressible viscous fluid for very large Reynolds numbers. *Proceedings of the royal society of London - series a: Mathematical and physical sciences* (Vol. 434(1890), 9–13).

Kraichnan, R. H. (1956). Pressure fluctuations in turbulent flow over a flat plate. *Journal of the Acoustical Society of America*, *28*(3), 378–390. https://doi.org/10.1121/1.1908336

Kunadi, A. S., Silberstein, R. P., & Thompson, S. E. (2024). Variation in zero plane displacement and roughness length for momentum revisited. *Boundary-Layer Meteorology*, *190*(8), 36. https://doi.org/10.1007/s10546-024-00876-8

Laemmel, T., Mohr, M., Longdoz, B., Schack-Kirchner, H., Lang, F., Schindler, D., & Maier, M. (2019). From above the forest into the soil–how wind affects soil gas transport through air pressure fluctuations. *Agricultural and Forest Meteorology*, *265*, 424–434. https://doi.org/10.1016/j.agrformet.2018.11.007

Launder, B. E., Reece, G. J., & Rodi, W. (1975). Progress in the development of a Reynolds-stress turbulence closure. *Journal of Fluid Mechanics*, *68*(3), 537–566. https://doi.org/10.1017/s0022112075001814

Maier, M., Schack-Kirchner, H., Hildebrand, E., & Holst, J. (2010). Pore-space CO_2 dynamics in a deep, well-aerated soil. *European Journal of Soil Science*, *61*(6), 877–887. https://doi.org/10.1111/j.1365-2389.2010.01287.x

Maitani, T., & Seo, T. (1985). Estimates of velocity-pressure and velocity-pressure gradient interactions in the surface layer over plant canopies. *Boundary-Layer Meteorology*, *33*(1), 51–60. https://doi.org/10.1007/bf00137035

Manes, C., Ridolfi, L., & Katul, G. (2012). A phenomenological model to describe turbulent friction in permeable-wall flows. *Geophysical Research Letters*, *39*(14). https://doi.org/10.1029/2012gl052369

Marty, J., Doury, B., & Kramer, A. (2021). Low and high broadband spectral models of atmospheric pressure fluctuation. *Journal of Atmospheric and Oceanic Technology*, *38*(10), 1813–1822. https://doi.org/10.1175/jtech-d-21-0006.1

Marusic, I., Monty, J., Hultmark, M., & Smits, A. (2013). On the logarithmic region in wall turbulence. *Journal of Fluid Mechanics*, *716*. R3. https://doi.org/10.1017/jfm.2012.511

Massman, W., Sommerfeld, R., Mosier, A., Zeller, K., Hehn, T., & Rochelle, S. (1997). A model investigation of turbulence-driven pressure-pumping effects on the rate of diffusion of CO_2, N_2O, and CH_4 through layered snowpacks. *Journal of Geophysical Research*, *102*(D15), 18851–18863. https://doi.org/10.1029/97jd00844

Massman, W., Sommerfeld, R., Zeller, K., Hehn, T., Hudnell, L., & Rochelle, S. (1995). CO_2 flux through a Wyoming seasonal snowpack: Diffusional and pressure pumping effects (Vol. 228, pp. 71–80). *IAHS Publications-Series of Proceedings and Reports-Intern Assoc Hydrological Sciences*.

Massman, W. J., & Frank, J. M. (2022). Modeling gas flow velocities in soils induced by variations in surface pressure, heat, and moisture dynamics. *Journal of Advances in Modeling Earth Systems*, *14*(10), e2022MS003086. https://doi.org/10.1029/2022ms003086

Mayor, S. D., Ayars, E., Scheive, K. A., Cobian, E., Frank, J. M., & Massman, W. J. (2023). Evaluation of the Infineon DPS310 for observations of turbulent pressure perturbations. In *103rd American meteorological society annual meeting*.

McBean, G. (1976). Scaling turbulence in the planetary boundary layer. *Atmosphere*, *14*(4), 254–267. https://doi.org/10.1080/00046973.1976.9648421

McBean, G., & Elliott, J. (1975). The vertical transports of kinetic energy by turbulence and pressure in the boundary layer. *Journal of the Atmospheric Sciences*, *32*(4), 753–766. https://doi.org/10.1175/1520-0469(1975)032<0753:tvtoke>2.0.co;2

Meriö, L.-J., Rauhala, A., Ala-aho, P., Kuzmin, A., Korpelainen, P., Kumpula, T., et al. (2023). Measuring the spatiotemporal variability in snow depth in subarctic environments using UASS–part 2: Snow processes and snow–canopy interactions. *The Cryosphere*, *17*(10), 4363–4380. https://doi.org/10.5194/tc-17-4363-2023

Miles, N. L., Wyngaard, J. C., & Otte, M. J. (2004). Turbulent pressure statistics in the atmospheric boundary layer from large-eddy simulation. *Boundary-Layer Meteorology*, *113*(2), 161–185. https://doi.org/10.1023/b:boun.0000039377.36809.1d

Monin, A. S., & Obukhov, A. M. (1954). Basic laws of turbulent mixing in the surface layer of the atmosphere. *Contributions of the Geophysical Institute, Slovak Academy of Sciences* (Vol. 151(163), e187), USSR.

Monin, A. S., & Yaglom, A. M. (1975). *Statistical fluid mechanics, Volume II: Mechanics of turbulence* (Vol. 2). MIT Press.

Mortarini, L., Katul, G. G., Cava, D., Dias-Junior, C. Q., Dias, N. L., Manzi, A., et al. (2023). Adjustments to the law of the wall above an amazon forest explained by a spectral link. *Physics of Fluids*, *35*(2). https://doi.org/10.1063/5.0135697

Obukhov, A., & Yaglom, A. (1959). On the microstructure of atmospheric turbulence–a review of recent work in the USSR. *Quarterly Journal of the Royal Meteorological Society*, *85*(364), 81–90. https://doi.org/10.1002/qj.49708536402

Ogura, Y., & Miyakoda, K. (1954). Note on the pressure fluctuations in isotropic turbulence. *Journal of the Meteorological Society of Japan. Ser. II*, *32*(5–6), 160–166. https://doi.org/10.2151/jmsj1923.32.5-6_160

Ould-Rouis, M., Antonia, R., Zhu, Y., & Anselmet, F. (1996). Turbulent pressure structure function. *Physical Review Letters*, *77*(11), 2222–2224. https://doi.org/10.1103/physrevlett.77.2222

Panton, R. L., & Linebarger, J. H. (1974). Wall pressure spectra calculations for equilibrium boundary layers. *Journal of Fluid Mechanics*, *65*(2), 261–287. https://doi.org/10.1017/s0022112074001388

Pearson, B., & Antonia, R. (2001). Reynolds-number dependence of turbulent velocity and pressure increments. *Journal of Fluid Mechanics*, *444*, 343–382. https://doi.org/10.1017/s0022112001005511

Phillips, O. M. (1957). On the generation of waves by turbulent wind. *Journal of Fluid Mechanics*, *2*(5), 417–445. https://doi.org/10.1017/s0022112057000233

Poggi, D., Porporato, A., Ridolfi, L., Albertson, J., & Katul, G. (2004). The effect of vegetation density on canopy sub-layer turbulence. *Boundary-Layer Meteorology*, *111*(3), 565–587. https://doi.org/10.1023/b:boun.0000016576.05621.73

Raspet, R., & Webster, J. (2015). Wind noise under a pine tree canopy. *Journal of the Acoustical Society of America*, *137*(2), 651–659. https://doi.org/10.1121/1.4906587

Raupach, M. R., Finnigan, J. J., & Brunet, Y. (1996). Coherent eddies and turbulence in vegetation canopies: The mixing-layer analogy. *Boundary-Layer Meteorology*, 351–382. https://doi.org/10.1007/978-94-017-0944-6_15

Roland, M., Vicca, S., Bahn, M., Ladreiter-Knauss, T., Schmitt, M., & Janssens, I. A. (2015). Importance of nondiffusive transport for soil CO_2 efflux in a temperate mountain grassland. *Journal of Geophysical Research: Biogeosciences*, *120*(3), 502–512. https://doi.org/10.1002/2014jg002788

Saddoughi, S., & Veeravalli, S. (1994). Local isotropy in turbulent boundary layers at high Reynolds number flow. *Journal of Fluid Mechanics*, *268*, 333–372. https://doi.org/10.1017/s0022112094001370

Sakai, R. K., Fitzjarrald, D. R., & Moore, K. E. (2001). Importance of low-frequency contributions to eddy fluxes observed over rough surfaces. *Journal of Applied Meteorology*, *40*(12), 2178–2192. https://doi.org/10.1175/1520-0450(2001)040<2178:iolfct>2.0.co;2

Salesky, S. T., Katul, G. G., & Chamecki, M. (2013). Buoyancy effects on the integral length scales and mean velocity profile in atmospheric surface layer flows. *Physics of Fluids*, *25*(10), 105101. https://doi.org/10.1063/1.4823747

Seok, B., Helmig, D., Williams, M. W., Liptzin, D., Chowanski, K., & Hueber, J. (2009). An automated system for continuous measurements of trace gas fluxes through snow: An evaluation of the gas diffusion method at a subalpine forest site, Niwot ridge, Colorado. *Biogeochemistry*, *95*(1), 95–113. https://doi.org/10.1007/s10533-009-9302-3

Shaw, R., & Zhang, X. (1992). Evidence of pressure-forced turbulent flow in a forest. *Boundary-Layer Meteorology*, *58*(3), 273–288. https://doi.org/10.1007/bf02033828

Sigmon, J., Knoerr, K., & Shaughnessy, E. (1983). Microscale pressure fluctuations in a mature deciduous forest. *Boundary-Layer Meteorology*, *27*(4), 345–358. https://doi.org/10.1007/bf02033744

Sorbjan, Z. (1989). *Structure of the atmospheric boundary layer*. Prentice Hall.

Stull, R. B. (2012). *An introduction to boundary layer meteorology* (Vol. 13). Springer Science and Business Media.

Suzuki, S., Ishizuka, S., Kitamura, K., Yamanoi, K., & Nakai, Y. (2006). Continuous estimation of winter carbon dioxide efflux from the snow surface in a deciduous broadleaf forest. *Journal of Geophysical Research*, *111*(D17). https://doi.org/10.1029/2005jd006595

Swanson, A. L., Lefer, B. L., Stroud, V., & Atlas, E. (2005). Trace gas emissions through a winter snowpack in the subalpine ecosystem at Niwot Ridge, Colorado. *Geophysical Research Letters*, *32*(3). https://doi.org/10.1029/2004gl021809

Takagi, K., Nomura, M., Ashiya, D., Takahashi, H., Sasa, K., Fujinuma, Y., et al. (2005). Dynamic carbon dioxide exchange through snowpack by wind-driven mass transfer in a conifer-broadleaf mixed forest in northernmost Japan. *Global Biogeochemical Cycles*, *19*(2). https://doi.org/10.1029/2004gb002272

Takle, E. S., Massman, W. J., Brandle, J. R., Schmidt, R., Zhou, X., Litvina, I. V., et al. (2004). Influence of high-frequency ambient pressure pumping on carbon dioxide efflux from soil. *Agricultural and Forest Meteorology*, *124*(3–4), 193–206. https://doi.org/10.1016/j.agrformet.2004.01.014

Taylor, G. I. (1938). The spectrum of turbulence. *Proceedings of the Royal Society of London - Series A: Mathematical and Physical Sciences* (Vol. 164(919), 476–490). https://doi.org/10.1098/rspa.1938.0032

Tennekes, H., & Lumley, J. (1972). *A first course in turbulence*. MIT Press.

Thomas, A., & Bull, M. (1983). On the role of wall-pressure fluctuations in deterministic motions in the turbulent boundary layer. *Journal of Fluid Mechanics*, *128*(-1), 283–322. https://doi.org/10.1017/s002211208300049x

Thomas, C., Mayer, J.-C., Meixner, F. X., & Foken, T. (2006). Analysis of low-frequency turbulence above tall vegetation using a Doppler sodar. *Boundary-Layer Meteorology*, *119*(3), 563–587. https://doi.org/10.1007/s10546-005-9038-0

Townsend, A. (1976). *The structure of turbulent shear flow*. Cambridge University press.

Tsuji, Y., Fransson, J. H., Alfredsson, P. H., & Johansson, A. V. (2007). Pressure statistics and their scaling in high-Reynolds-number turbulent boundary layers. *Journal of Fluid Mechanics*, *585*, 1–40. https://doi.org/10.1017/s0022112007006076

Tsuji, Y., & Ishihara, T. (2003). Similarity scaling of pressure fluctuation in turbulence. *Physical Review E*, *68*(2), 026309. https://doi.org/10.1103/physreve.68.026309

Uberoi, M. (1953). Quadruple velocity correlations and pressure fluctuations in isotropic turbulence. *Journal of the Aeronautical Sciences*, *20*(3), 197–204. https://doi.org/10.2514/8.2589

Waterman, T., Bragg, A. D., Katul, G., & Chaney, N. (2022). Examining parameterizations of potential temperature variance across varied landscapes for use in earth system models. *Journal of Geophysical Research: Atmospheres*, *127*(8), e2021JD036236. https://doi.org/10.1029/2021jd036236

Wei, Z., Zhang, H., Ren, Y., Li, Q., Cai, X., Song, Y., & Kang, L. (2021). Study on the characteristics of the pressure fluctuations and their contribution to turbulence kinetic energy. *Atmospheric Research*, *258*, 105634. https://doi.org/10.1016/j.atmosres.2021.105634

Wilczak, J., & Businger, J. A. (1984). Large-scale eddies in the unstably stratified atmospheric surface layer. Part II: Turbulent pressure fluctuations and the budgets of heat flux, stress and turbulent kinetic energy. *Journal of the Atmospheric Sciences*, *41*(24), 3551–3567. https://doi.org/10.1175/1520-0469(1984)041<3551:lseitu>2.0.co;2

Willmarth, W. (1975). Pressure fluctuations beneath turbulent boundary layers. *Annual Review of Fluid Mechanics*, *7*(1), 13–36. https://doi.org/10.1146/annurev.fl.07.010175.000305

Wyngaard, J., & Clifford, S. (1977). Taylor's hypothesis and high–frequency turbulence spectra. *Journal of the Atmospheric Sciences*, *34*(6), 922–929. https://doi.org/10.1175/1520-0469(1977)034<0922:thahts>2.0.co;2

Wyngaard, J., & Coté, O. (1971). The budgets of turbulent kinetic energy and temperature variance in the atmospheric surface layer. *Journal of the Atmospheric Sciences*, *28*(2), 190–201. https://doi.org/10.1175/1520-0469(1971)028<0190:tbotke>2.0.co;2

Xu, H., Ouellette, N. T., Vincenzi, D., & Bodenschatz, E. (2007). Acceleration correlations and pressure structure functions in high-Reynolds number turbulence. *Physical Review Letters*, *99*(20), 204501. https://doi.org/10.1103/physrevlett.99.204501

Zahn, E., Bou-Zeid, E., Good, S. P., Katul, G. G., Thomas, C. K., Ghannam, K., et al. (2022). Direct partitioning of eddy-covariance water and carbon dioxide fluxes into ground and plant components. *Agricultural and Forest Meteorology*, *315*, 108790. https://doi.org/10.1016/j.agrformet.2021.108790

Zhao, S., Cheng, E., Qiu, X., Burnett, I., & Liu, J. C.-c. (2016). Pressure spectra in turbulent flows in the inertial and the dissipation ranges. *Journal of the Acoustical Society of America*, *140*(6), 4178–4182. https://doi.org/10.1121/1.4968881

Zhuang, Y., & Amiro, B. (1994). Pressure fluctuations during coherent motions and their effects on the budgets of turbulent kinetic energy and momentum flux within a forest canopy. *Journal of Applied Meteorology and Climatology*, *33*(6), 704–711. https://doi.org/10.1175/1520-0450(1994)033<0704:pfdcma>2.0.co;2

Erratum

The originally published version of this article contained errors in Equations 15–18 and related text. Equations 15–18 have been corrected as follows: $\frac{E_{pp}(k_x)}{\epsilon^{4/3}L_p^{7/3}} = \phi_L(k_xL_p)$, $\phi_L(k_xL_p) = \frac{E_{pp}(k_x)}{\epsilon^{4/3}L_p^{7/3}} = \frac{A_o}{k_xL_p}$, $E_{pp}(k_x) = A_o\epsilon^{4/3}L_p^{7/3}(k_xL_p)^{-1} = C_{p2}\left(\frac{u_*^3}{L_p}\right)^{4/3}L_p^{7/3}\left(\frac{1}{k_xL_p}\right)$, $E_{pp}(k_x) = C_{p2}u_*^4\,k_x^{-1}$. The phrase and sentence immediately following Equation 16 have been corrected to the following: "where A_o is a similarity coefficient and ϵ scales as $u_*^2(u_*/L_p)$. This choice of ϕ_L leads to a model for the pressure spectrum at large scales given by …" The sentence immediately following Equation 17 has been corrected to the following: "where C_{p2} is another similarity coefficient. With this choice for $\phi_p(k_xL_p)$, Equation 15 reduces to …." This may be considered the authoritative version of record.